Analysis of Boron Doped Hydrogenated Amorphous Silicon Carbide Thin Film for Silicon Heterojunction Solar Cells

A THESIS SUBMITTED TO
THE GRADUATE SCHOOL OF NATURAL AND APPLIED SCIENCES
OF
MIDDLE EAST TECHNICAL UNIVERSITY

BY

ARGHAVAN SALIMI

IN PARTIAL FULFILLMENT OF THE REQUIREMENTS
FOR
THE DEGREE OF MASTER OF SCIENCE
IN
MICRO AND NANOTECHNOLOGY

SEPTEMBER 2019

Approval of the thesis:

ANALYSIS OF BORON DOPED HYDROGENATED AMORPHOUS SILICON CARBIDE THIN FILM FOR SILICON HETEROJUNCTION SOLAR CELLS

submitted by **ARGHAVAN SALIMI** in partial fulfillment of the requirements for the degree of **Master of Science in Micro and Nanotechnology Department, Middle East Technical University** by,

Prof. Dr. Halil Kalıpçılar
Dean, Graduate School of **Natural and Applied Sciences** _____

Prof. Dr. Almıla Güvenç Yazıcıoğlu
Head of Department, **Micro and Nanotechnology** _____

Prof. Dr. Raşit Turan
Supervisor, **Micro and Nanotechnology, METU** _____

Assist. Prof. Dr. Selçuk Yerci
Co-Supervisor, **Electric and Electronic Engineering, METU** _____

Examining Committee Members:

Assoc. Prof. Dr. Akın Bacıoğlu Mustafa Kulakcı
Physics Engineering, Hacettepe University _____

Prof. Dr. Raşit Turan
Micro and Nanotechnology, METU _____

Assist. Prof. Dr. Serdar Kocaman
Electric and Electronic Engineering, METU _____

Assist. Prof. Dr. Demet Asil Alptekin
Chemistry, METU _____

Assoc. Prof. Dr. Mustafa Kulakcı
Physics, Eskişehir Technical University _____

Date: 05.09.2019

I hereby declare that all information in this document has been obtained and presented in accordance with academic rules and ethical conduct. I also declare that, as required by these rules and conduct, I have fully cited and referenced all material and results that are not original to this work.

Name, Surname: Arghavan Salimi

Signature:

ABSTRACT

ANALYSIS OF BORON DOPED HYDROGENATED AMORPHOUS SILICON CARBIDE THIN FILM FOR SILICON HETEROJUNCTION SOLAR CELLS

Salimi, Arghavan
Master of Science, Micro and Nanotechnology
Supervisor: Prof. Dr. Raşit Turan
Co-Supervisor: Assist. Prof. Dr. Selçuk Yerci

September 2019, 90 pages

Silicon based solar cells are the dominant type of solar cells in the photovoltaic industry. Recently, there have been increasing efforts to develop c-Si solar cells with higher efficiency and lower cost. Among them, silicon heterojunction solar cell (SHJ) is attracting much attention because of its superior performance values demonstrated at both R&D and industrial levels. One of the common limiting criteria is the recombination at the front side which can be solved by providing proper passivation at the front contact. In case of amorphous silicon (a-Si), the parasitic absorption of photons and recombination of the minority carriers are considerably high, thus, one approach can be increasing its optical band gap to overcome these impediments. One way to increase the optical band gap of a-Si is adding carbon(C) during boron(B) doping and hydrogenating amorphous silicon (a-Si:H). Generally, the p-type a-Si:H optical band gap is around 1.6 eV which is close to the intrinsic a-Si:H optical band gap. Meanwhile, C alloying allows us to increase the optical band gap from 1.6 up to 2.4 eV. In this work, we tried to increase the optical band gap of B doped a-Si:H deposited by PECVD through introducing C into the structure. We modified the deposition parameters such as deposition temperature, RF power of PECVD, and precursors gas flow rates to see their effects on the doping, a-Si:H optical band gap,

and amount of C introduced into the structure. The best characteristic parameters that we have achieved for p-a-SiC:H is optical band gap of 1.89 eV with dark conductivity of 1.8×10^{-5} $(\Omega.cm)^{-1}$. By increasing the RF-power, we have observed that the methane molecules decompose better and C atom incorporates into the structure. Also, increasing the methane flow rate improved the C incorporation within the structure.

Keywords: Silicon solar cells, Heterojunction solar cells, Hydrogenated amorphous silicon solar cells, Boron doping, Boron doped amorphous silicon carbide

ÖZ

Bor Katkılı Hidrojene Amorf Silisyum Karbon Katmanının Silisyum Heterojunction Güneş Pilleri için Analizi

Salimi, Arghavan
Yüksek Lisans, Mikro ve Nanoteknoloji
Tez Danışmanı: Prof. Dr. Raşit Turan
Ortak Tez Danışmanı: Dr. Öğr. Üyesi Selçuk Yerci

Eylül 2019, 90 sayfa

Fotovoltaik endüstrisinde baskın olan güneş hücreleri silisyum bazlı güneş hücreleridir. Son zamanlarda, daha yüksek verimlilik ve daha düşük maliyetle c-Si güneş pilleri geliştirme çabaları artmaktadır. Bunlar arasında, silisyum hetero eklem guneş hücresi (SHJ), hem Ar-Ge hem de endüstriyel seviyelerde gösterilen üstün performans değerleri nedeniyle çok dikkat çekmektedir. silisyum güneş hücresini sınırlayan kriterlerinden biri, ön yüzeyde uygun pasivasyon sağlayarak çözülebilen ön kısımdaki yeniden birleşmedir. Amorf silisyum (a-Si) durumunda ise, fotonların parazitik emilimi ve azınlık taşıyıcıların yeniden birleşmesi oldukça yüksektir, dolayısıyla bu engellerin üstesinden gelmek için bant aralığını artırılması yaklaşımlardan birisidir. Amorf silisyum bant aralığını arttırmanın bir yolu, bor katkılama işlemi sırasında karbon ekleme ve amorf silisyum hidrojenlenmesi (a-Si: H). Genel olarak, p-tipi a-Si bant aralığı, yaklaşık 1,6 eV civarında ve a-Si bant aralığına yakındır. Bu arada, karbon alaşımları sayesinde bant aralığı 1,6 eV'dan 2,4 eV'a çıkarmamızı sağlamaktadır. Silisyumdaki bor difüzyonu zorlu bir konu olmasına rağmen, bor hala p-tipi amorf silisyum için hâkim bir katkı maddesidir. Bu çalışmada, PECVD tarafından biriktirilen boron'un a-Si: H katkılı bant yapısını yapıya karbon katmak suretiyle arttırmaya çalıştık. Üretim sıcaklığı, PECVD'nin RF gücü ve gaz akış

hızlarının katkılama, a-Si: H bant aralığı ve yapıya verilen Karbon miktarına olan etkisini görmek için çökeltme parametrelerini değiştirdik. P-aSiC üretimi sonucunda elde ettiğimiz en iyi değer optik bant aralığı 1,89eV ve karanlık iletkenliği $1{,}8\times10^{-5}$ $(\Omega.\mathrm{cm})^{-1}$ olarak bulunmuştur. Üretim gücü arrtırıldığında metan molekülleri daha iyi ayrışırken amorf matrise karbon bağlanmaktadır. Metan akış miktarındaki artış sistem içersine C bağlanmasını arttırmaktadır.

Anahtar Kelimeler: Silisyum güneş hücreleri, Heteroeklem güneş gözeleri , Amorf silisyum hidrojenlenmesi güneş gözeleri, Bor katkılı amorf silisyum karbün

To my dearest dear and my family who support me all the times

ACKNOWLEDGEMENTS

I want to specially thank my advisor Prof. Dr. Raşit Turan for his ultimate support and giving me opportunity to work at GÜNAM. I want to thank my daily supervisor Ergi Dönerçark for his kind assistance and consultation during my experiences. I want to thank my family for supporting me and bear with me all these times. I acknowledge Dr. Ismail Kabaçelik, Hande Çiftpinar, and Seçil Çüler for their contribution and help in my experiences.

TABLE OF CONTENTS

LIST OF TABLES

TABLES

LIST OF FIGURES

FIGURES

LIST OF ABBREVIATIONS

a-Si:H	Hydrogenated amorphous Silicon
c-Si	Crystalline Silicon
CVD	Chemical vapor deposition
DI Water	Deionized water
DSSC	Dye sensitized solar cells
E_C	Energy of conduction band
E_G	Band gap energy
EHP	Electron-hole pair
EQE	External quantum efficiency
E_V	Energy of valance band
FF	Fill factor
HCl	Hydrochloric acid
HF	Hydrofluoric acid
p-a-SiC:H	Hydrogenated p type amorphous Silicon Carbide
p-a-Si:H	Hydrogenated p type amorphous Silicon
PECVD	Plasma enhanced chemical vapor deposition

LIST OF SYMBOLS

α	Absorption coefficient
Al	Aluminum
B_2H_6	Diborane
CH_4	Methane
H_2	Hydrogen
J_{SC}	Short-circuit current
k_B	Boltzmann constant
R_s	Series resistance
R_{sh}	Shunt resistance
SiH_4	Silane
T	Temperature
V_{OC}	Open-circuit voltage

CHAPTER 1

INTRODUCTION

1.1. Photovoltaic Technology

Direct conversion of solar energy into the electrical energy is called photovoltaic effect which is discovered by French physicist Edmond Becquerel in 1839. The starting point of photovoltaic technology dates back to 1839 when the French physicist Edmond Becquerel discovered photovoltaic effect and the operation of solar cell[1]. In 1905 Albert Einstein explained the photoelectric effect by finding a quantum theory on light and in 1921, this discovery won him a Nobel prize[2]. Russel Ohl patented the first silicon photosensitive device at 1941[3] and in 1954, the researchers, Chapin, Fuller and Pearson reported the first silicon solar cell with 6 % efficiency in Bell Labs[4]. In the second half of the last century, the rate of the developments and discoveries of silicon solar cell technology speeds up, currently, more than 25 % efficiency has been achieved in silicon heterostructure (HIT) technology by Kaneka which is a Japanese company [5]. Also, more that 26.1 % efficiency is introduced by Fraunhofer Institute for TOPC on IBC solar cells[6].

The energy obtained from sunlight is amongst the cleanest forms of renewable energy sources since the process of its generation makes minimum amount of pollution such as greenhouse gases. In the days when photovoltaic technology was first introduced, around 50 years ago, the energy consumed to produce a PV panel was way more than the amount of energy produced by the panel during its lifetime. Nevertheless, in the passing decade, the efficiency rates of the panels and the solar cells has gone up considerably and many novel manufacturing methods has been introduced to the industry, causing the payback time to reduce to 3–5 years, depending on the amount of sunlight available at the site which panels have been installed in [7].

1.1.1. Solar Cell Generation

1.1.1.1. First Generation Solar Cells

Multi-crystalline and single crystalline or monocrystalline silicon solar cells are the first-generation solar cells that had been introduced to the industry and both are considered as wafer-based technologies shown in Figure 1.1. Currently, multi-crystalline solar cell has the highest rate of production compared to other solar cell technologies in the market. The reason for that is even though single crystalline silicon solar cells holds higher efficiency rates than the multi-crystalline silicon solar cells, the cost of production for single crystalline silicon solar cells is much higher compared to the multi-crystalline cells and therefore multi-crystalline cells dominate today's market.

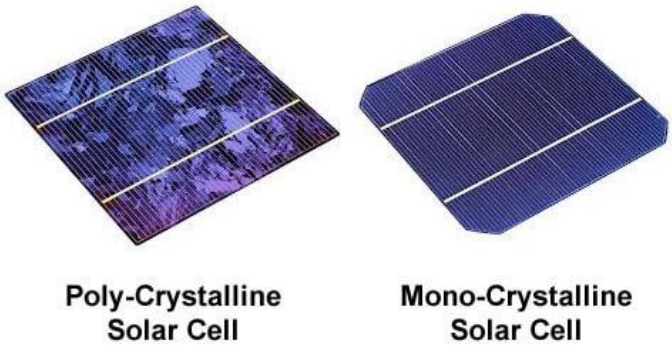

Figure 1.1. Industrial Poly-Crystalline and Mono-Crystalline solar cells[8]

Today, first generation silicon solar cells wafers have reached an efficiency of around 24% and for the case of installed solar cell panels the efficiency is around 19%. These numbers have been achieved by implementing various doping and metallization methods in order to reduce the defect states and shading effects. A few of these methods are Emitter Wrap Through (EWT), Metal Wrap Through (MWT) and Interdigitated Back Contact (IBC) design which are shown in Figure 2.1.

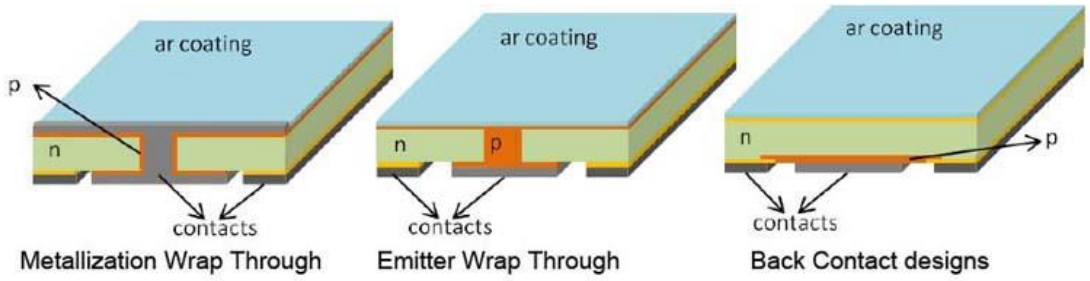

Figure 1.2. Metallization Wrap Through- Emitter Wrap Through- Back Contact designs [9]

1.1.1.2. Second Generation Solar Cells

Thin film solar cells are considered to be second generation photovoltaic cells, these thin films are generated by depositing a very thin layer of the material on thicker carriers or substrates, deposited as a thin layer of photovoltaic material on thicker substrates. Some example for the second-generation solar cells are a-Si solar cells, Cd-Te solar cells and CIGS solar cells.

Manufacturing thin films are cheaper since the amount of material used to produce thin films is much less than what is used in conventional cells. However, as a downside, depositing thin films on sizeable areas is very challenging and is one of the main issues that thin film industry encounters these days. Moreover, thin film solar cells have lower amounts of efficiency when compared to regular wafer based solar cells. However, regardless of all these drawbacks, being cost efficient and easily deposited on various substrates make this technology advantageous compared to first generation cells.

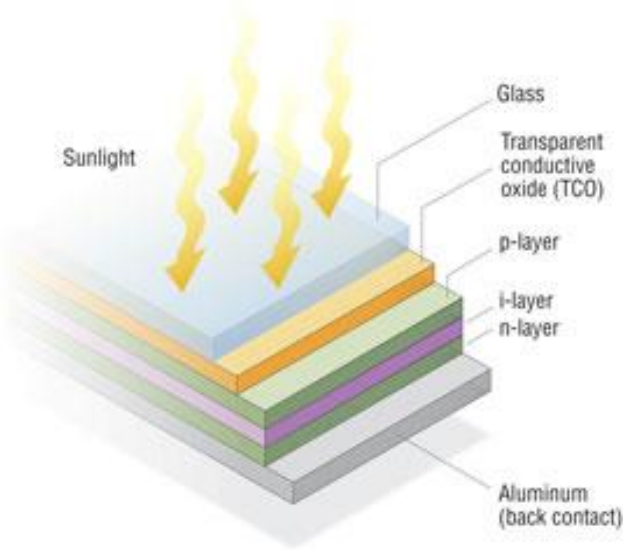

Figure 1.3. Thin film amorphous Silicon solar cell [10]

1.1.1.3. Third Generation Solar Cells

The last generation of solar cells include a variety of novel solar cell type like group III-V semiconductors (tandem cells), organic solar cells, dye sensitized and perovskite solar cells.

III-V compound semiconductors are obtained by combining group III elements with group V elements. Examples for this type of semiconductors are GaAs, InAs, InP. These semiconductors can be used to achieve various bandgaps. These semiconductors can be grown on each other with different bandgaps and the solar cell made from them can absorb a wide range of solar spectrum. However, manufacturing of these materials can be rather costly, therefore these types of solar cells are typically utilized in Concentrated Photovoltaic (CPV) and space-satellite applications. In CPV sunlight concentrated through relatively cheap lens on to the small area cell in a concentration factor between 10’s to 1000’s. Achieved highest efficiency from these cells under concentrated light with a factor of 143 is around %47. Due to their high efficiency, high radiation and temperature tolerances, III-V cells are indispensable for space applications where watt/kg is much important rather than price.

Organic solar cells are manufactured using inexpensive polymers and since the absorption rates are very high, their deposition as ultra-thin layers are possible. Hence, they are considered as the most cost-efficient solar cells that can be manufactured. Nevertheless, the efficiency gained by organic solar cells are rather low. The highest efficiency reached with organic solar cells is about 16.5% [11]. Considering all this, organic solar cells are still used because of their applicability to large areas and on flexible substrates with roll to roll (R2R) production method.

Dye sensitized solar cells (DSSC) is a type of a solar cell which is containing dye molecules on the titanium dioxide (TiO_2) nanoparticles. Efficiency values up to 11.9 % have been reported for DSSC. Low cost production makes this type of solar cells preferable than others. However, the light degradation of the solar cells increase the recombination of the carriers. On the other hand, the transparency and flexibility of the DSSC solar cells make it applicable in integrating them on the facet of buildings[12].

1.2. Silicon Heterojunction Solar Cell (SHJ)

In a solar cell, electrical energy production consists of three steps. First, the energy absorbed from sun transforms into an energy which is the concentration of positive (hole) and negative charges (electron) inside the semiconducting material. Then, the generated electron-hole pairs (EHP) get separated and each one gets collected at the two ends of the solar cells and electrical energy is generated. Electron-hole pairs have rather short lifetime and in order to obtain high efficiencies from the solar cell technology the majority of this EHP must be collected before getting recombined. Therefore, the thickness of the solar cell cannot exceed a certain length and must be shorter than the length the carriers can travel before recombination happens[13].

In order to efficiently separate EHP generated inside the light absorbing bulk, some layers must be applied on the bulk. The issue with these layers is that they should allow the passage of only one type of this carrier charges while blocking the other one[13]. Therefore, the conventional solar cells (which have two parts) are made from

two different doping types. If the two parts are made from the same material it is called Homojunction, otherwise it is called Heterojunction.

Nearly all the solar cells benefit from the p-n junction. In order to separate the carriers, the p-n junction is necessary. For homojunction by doping, the Si p-type and n-type layers can be created. For Si solar cell doping can be done by diffusion or implanting. Solid state diffusion is a common method for introducing dopant atoms into the semiconductor[14]. The Si substrate can be doped by phosphorous atoms (n-type) and by doping with boron atoms, p-type can be formed.

Depositing p-type a-Si and the n-type a-Si on the c-Si instead of the diffused junction lead to increase the band bending and separate the charge carriers even more. The possible recombination centers at the interface of c-Si and metal contact is pushed away from the bulk c-Si which decrease the recombination of the carriers. The recombination states at the surface of the c-Si are mainly due to the dangling bonds on the surface. One solution is depositing a thin layer of intrinsic a-Si on the c-Si, which will decrease the dangling bonds by passivating them.

Heterojunction (HJ) Si solar cells consist of crystal Si wafers and amorphous thin si layers. C-Si wafers are used for absorbing sunlight and transporting carriers, and amorphous thin layers for passivating the dangling bonds and forming the p-n junction. Main advantage of SHJ solar cells are that high power conversion efficiency and low temperatures (below 200 °C) deposition which allows thin Si wafers (around 100 µm) to be produced[15][13]. The highest record efficiency so far for single-junction c-Si is reported by Kaneka for 26.7%[15]. There are several studies regarding the efficient doping of the p and n-type layers in order to enhance the band bending of the c-Si and a-Si and enhanced carrier selective collection [15]. One way to enhance the efficiency of the p-type a-Si is to lower the optical loses (parasitic absorption) by increasing the band gap and making it more transparent [16].

1.3. Hydrogenated Amorphous Silicon Carbide

Hydrogenated amorphous Silicon Carbide(a-SiC:H) takes part in a wide range of applications beside the PV technology. Biomedical, IC fields, and optoelectronics (LED, optical sensors) are some of the fields that it can be used[17]. There are different deposition techniques for a-SiC:H such as metal organic chemical vapor deposition (MOCVD), hot wire chemical vapor deposition (HWCVD), PECVD, and reactive magnetron co-sputtering. Radio frequency PECVD (RF-PECVD) provides low temperature deposition and widely used in the industrial applications [18]. A-SiC:H in general fabricated by RF-PECVD by introducing Carbon bearing hydrides gases such as Methane (CH_4) to Silane (SiH_4) and Hydrogen gases. For N-Type doping, Phosphine (PH_3) and for P-Type doping, Diborane (B_2H_6) and Trimethyl boron ($B(CH_3)$) are used [13].

Advantages of a-SiC:H in optical, thermal, electrical, and structural properties make it favorable to use as the window layer and emitter layer in SHJ solar cells. A-SiC:H passivates the dangling bonds of c-Si because of H content. Parasitic absorption of the layer is high when the optical band gap is low by increasing the optical band gap the parasitic absorption decreases. Optical band gap of a-SiC:H can be tuned in range of 1.8-3.85 eV, which is dependent in the C content of the layer [19]. Increasing C content leads to decrease in the electrical properties because of enlarging disorder in the amorphous network. Having an ideal structure of a-SiC would be that the Si is only bonded with C. However, during deposition specially at low temperatures C happens to bond randomly in the structure or make clusters [20].

The reason is that the binding energy of Si-C (4.6 eV) bond is higher than Si-Si(1.79eV) make it less likely to happen during the deposition[20]. In addition to reaching an atomic ordering during the deposition, formation of void clusters (vicinities within the structure) are also probable in a-SiC:H deposited thin films[21]. Studies have shown that H_2 dilution during deposition has been improved the structural defects significantly[22][23]. Also, studies on the annealing doped and

undoped a-SiC:H showed that annealing at 300 °C temperature and higher, H starts to effuse from the structure. This lead to increase the defects within the structure and an immediate life time reduction [24].

Another study on the a-Si based n-i-p solar cell showed that replacing the p-type a-Si:H window layer by p-type a-SiC:H layer and H plasma treatment at the interfaces, improve the performance of the solar cell. Madaka et.al. studied the effect of variation CH_4 flow rate in structure of the p-a-SiC:H deposited by PECVD on flexible polyethylene terephthalate (PET) at low temperatures[18]. Optical and electrical characteristics of the p type window layer investigated as well. They have employed different characterization techniques such as ellipsometry, Raman, FTIR.

They have observed that the thickness of the thin film decreases as the CH_4 flow rate increases. The explanation was the weak bond of H from the surface etched by CH_n radicals. Moreover, the unsaturated bonds within the structure bonded with C atoms which lead to increase the optical band gap.

From FTIR spectra bonds related to the Si-C and C-H_n are detected. Then the intensity of the Si-H, Si-C, and C-H are calculated. The density of the C-H and Si-C increased by increasing the CH_4 flow rate. Furthermore, the performance of the solar cell was enhanced by H plasma treatment before depositing i-a-Si:H and p-a-SiC:H.

Total improvement in the solar cell was due to the reduction of series resistance and to the enhancement of the shunt resistance, V_{oc} ,J_{sc} , and FF which in turn improved the external quantum efficiency (EQE) of the solar cell as shown in Figure1.4 [18].

	Substrate	R_s (Ω-cm^2)	R_{sh} (Ω-cm^2)	V_{oc} (mV)	J_{sc} (mA/cm^2)	FF	η (%)
Case (i): *a-Si:H(p)* + without HPT at *n/i* & *i/p* interface	PET	19.68	1519.90	795	7.14	0.58	3.30
	PI	25.35	984.37	782	7.41	0.58	3.36
	glass	16.91	1058.82	794	7.94	0.59	3.82
Case (ii): *a-Si:H(p)* + with HPT at *n/i* & *i/p* interface	PET	18.08	1344.00	801	7.16	0.6	3.48
	PI	19.78	1460.02	796	7.88	0.58	3.64
	glass	16.32	1565.21	798	8.29	0.61	4.00
Case (iii): *a-SiC:H(p)* + with HPT at *n/i* & *i/p* interface	PET	15.53	2183.71	809	7.44	0.61	3.66
	PI	18.86	1869.43	811	7.94	0.63	4.06
	glass	15.54	2146.50	810	8.61	0.62	4.27

Figure 1.4. Medaka et al. published these values of series resistance(R_s), shunt resistance (R_{sh}), open circuit voltage (V_{oc}), short circuit current(J_{sh}), fill factor(FF) and efficiency (%) for their n-i-p solar cell deposited on flexible PET,PI and glass substrates[18]

1.3.1. Structural Network

Although there are several studies regarding the a-SiC structure, however, it is still unknown. One of the theories that explains the amorphous network is continuous random network proposed (CNR)by Polk in 1971. This theory is proposed for amorphous semiconductors and their alloys. Polk's theory proposed that the amorphous network is in tetrahedral arrangement as same as the crystalline form of the element but with different bond lengths and angles and there is no long-range order[25].

In another way, it means that in the short range the amorphous atoms placed in a configuration that they are surrounded by the same neighbor atoms as in the crystalline form. However, in the long range they do not have the periodic structure which is the main characteristic for the crystalline lattice as shown in the Figure 1.5[20].

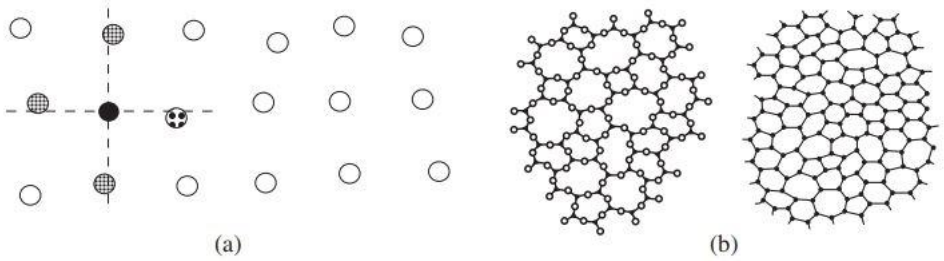

*Figure 1.5.*Schematic of two dimensional structure of a-Si network similar to the Crystalline (a)short order (b) diagram of the a-Si network which has no short order arrangement [20]

However, based on some simulation studies the network of a-SiC does not have the ideal tetrahedral geometry because of the C[26]. C atoms within the structure of the a-Si can arrange in a way that they form graphite and diamond like C-C bonds, which these structures have been observed in several studies[27][28][19]. There are some simulation studies investigating the effect of atomic concentration of Si and C atoms present in the structure and how it affects the forming Si-Si and C-C bonds (graphite and diamond) within the structure which deviate from the ideal tetrahedral structure[29].

The studies investigated atomic concentration within the structure, annealing effect for the crystalline form and also the effect of deposition condition[30]. The Si atoms in the amorphous structure have tendency to form tetrahedral bonding (Si-C) in addition they will form Si-Si bonds as well. However C atoms depending on the deposition conditions may form different bonds (Si-C, graphite like C-C, diamond like) [27].

1.3.2. Hydrogen Incorporation

Studies showed that the H corporation into the a-Si structure has significant effects in the structure for example internal stress of the structure and also bonding configuration, particularly passivation of the possible defect states within the structure[31]. The defect density of a-Si deposited without H is excessively high (around 10^{19} defects/cm^3) which make it impractical as a device material[31]. On the other hand, a-Si deposited with H can have defect densities around 10^6 defects/cm^3

[31]. A-Si:H can be deposited by different fabrication methods such as SiH_4 decomposition on a hot wire, sputtering Si in Argon-H_2 atmosphere, and plasma enhanced chemical vapor deposition (PECVD). Regardless of the deposition method, the improvement of the optical and electrical behavior depends on the H content and how it is incorporated in the structure[31].

H bonding stability in the amorphous network plays an important role on the passivation quality and light-induced degradation. A-Si deposited in high H_2 dilution has low light induced degradation [32][33]. H incorporation in the a-Si structure can be detected by various characterization techniques such as infrared absorption and electron paramagnetic resonance. Fourier transform infrared spectroscopy (FTIR) is used frequently in the H content determination inside the a-Si:H network. H can exist in various configuration within the amorphous network; it can be bonded to Si or another H atom and also, can appear as H_2 molecules. Only the Si-H bond is an infrared active which is detected by the FTIR spectrometer[32].

From the FTIR results for high Hydrogen dilution, the Si-H related vibrational bonds frequency may shift as the dilution increases. The Wagging mode shifts to lower wavenumbers and the stretching bond may shift to higher wavenumbers[32][34].

Depositing a-SiC alloy with high H_2 dilution by RF PECVD has been studied to see the effect of H in the network of the a-SiC. Interesting results are achieved such as the tendency of the amorphous network toward the c-SiC structure. Pereya et al. investigated the SiH_4 starving plasma deposition and altering the RF power and H_2 dilution to achieve this network of a-SiC[33]. In this paper they achieved high optical band gap a-SiC:H with low power and low silane ratio in order to achieve diamond like C-C bonds instead of graphite like bonds which indicates that diamond like bonds lead to higher optical band gap.

Ross et al. applied Multiple Internal Reflection Infrared Spectroscopy (MIR-IR) as a characterization method for a-Si:H grown by PECVD[35]. Their analyses raveled the properties of B doping and H_2 dilution in the bond structure of the a-Si. They have

observed that by increasing the doping ratio the Si-H bond decrease in absorption intensity. Moreover, by increasing the H_2 flow rate during deposition of absorption intensity of B doped a-Si the B-H bond decrease. B doping efficiency is lower in a-Si rather than c-Si which may be due to several reasons. They have stated that some studies revealed that one of the reasons for non-active B doping could be the Hatom passivating the B atom. They have observed different bonds related to the B and H bonding such as B-H, BH_2, BH_3, Si-H-B in their MIR-IR results. Further results from the conductivity measurements revealed that increasing doping ratio from 0.13 did not contribute to improve the conductivity and did not act as active dopants. However, MIR-IR results showed that increasing doping ratio up to 0.32 contribute to the B-H bond. Thereby, they concluded that the further increasing of doping ratio increases the B-H bond in the structure and excess B atoms act as the non-active dopants[35].

1.3.3. Carbon Incorporation

C as an impurity in the thin films will act as a defect state and it is one of the most avoided elements in the deposition processes. However, the controlled incorporation of C in the a-SiC network can lead to band gap tuning for the a-SiC. It is expected to see that the increase in the C incorporation will increase the band gap. However, for higher C incorporation in the thin film, reaching higher band gap energies (E_{BG}>2.5-3eV) is hard to achieve[33]. This can be due to the more graphite like bonding of C-C rather than diamond like C-C bonds. They demonstrated that in the SiH_4 starving condition in which the RF power is kept low and the SiH_4 flow rate is low as well and the deposition is controlled by SiH_4 radicals and make enough time for C incorporation with C-C diamond like bindings(similar to c-Si-C) which they achieved high band gap (3.5eV) for a-SiC. They deducted from several characteristics measurements such as FTIR with comparing the Si-C bond and Si-H and Si-CH_3 bonds that the a-SiC:H deposited in the starving condition plus H_2 dilution show the short-range order structure characteristics similar to C-SiC[33].

1.3.4. Dopant Incorporation

Doping is a crucial step for both a-Si and c-Si in device fabrications. However, doping a-Si is lower than c-Si due to the structural characteristics of a-Si [20]. In doping process of a-Si, H is a necessary precursor beside SiH_4, moreover H atoms passivate the dangling bonds in the structure. For doping the mixture of SiH_4 and H is used with the dopant gas precursor which in case of N-Type doping, phosphine (PH_3) and for P-Type doping, diborane (B_2H_6) and trimethyl boron ($B(CH_3)$) are used[13]. The suggested doping elements for n-type a-SiC are Nitrogen and Phosphorous atoms and for p-type are Aluminum and B atoms [33].

In C-Si the dopant atoms have a four-fold coordination in the structure and make it electrically conductive. This structure is also, expected to happen in the amorphous structure in order to be electrically conductive. However, the dopants may have various configurations in the amorphous structure because of the random network of amorphous Si. In addition, the present H atoms can make bonds with dopant atoms and they cannot be electrically active in the structure[13].

Furthermore, as the doping level increases the efficiency of doping decreases makes it harder to dope a-Si. This can be explained by the structural properties of the a-Si. In the c-Si, as the doping increase the fermi level (E_f) gets closer to the Conduction energy band (E_c) or Valance energy band (E_v). However, for a-Si by increasing the doping the E_f does not get closer to the energy band edges. The band diagram of the a-Si and c-Si are shown in the Figure 1.6 and Figure 1.7. As the fermi energy level gets closer to the energy bands it is facing the band tails. Most of the carriers injected by the dopants will fill up the band tail states, and really small portion of these carriers will be as free electrons and holes.

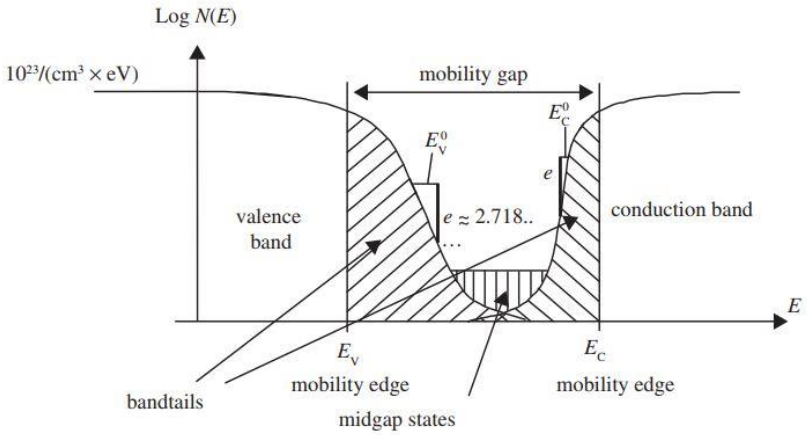

Figure 1.6. Schematically drawing of the mobility gap state in the amorphous semiconductors. LogN(E) is density of states in logarithmic scale and E is the electronic states. Gap states are within the mobility edge of the E_c and E_v[36]

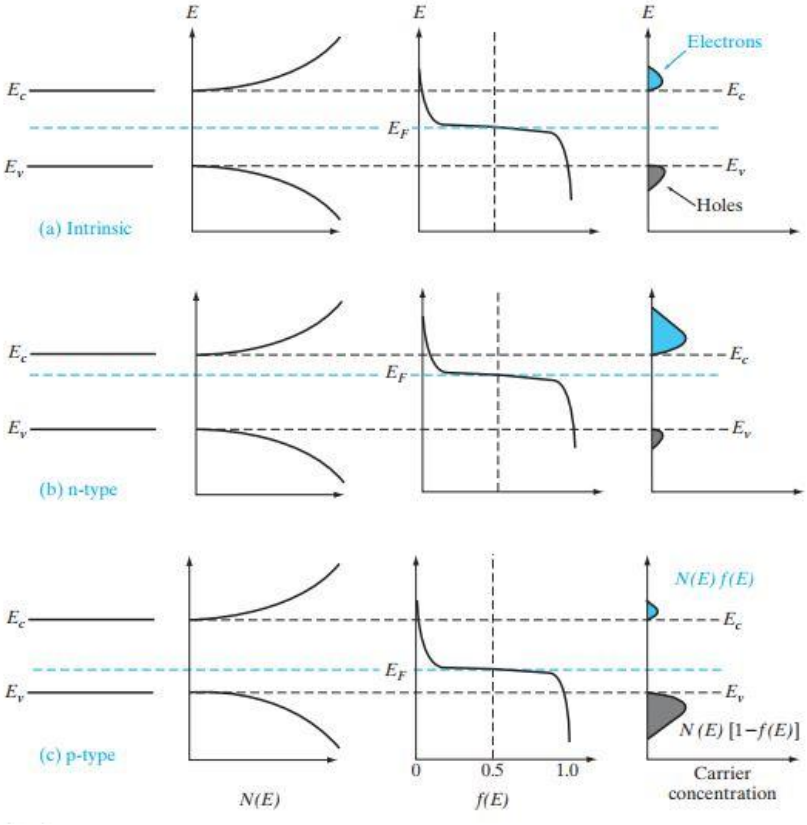

Figure 1.7. Schematic band diagram, Fermi-Dirac distribution, carrier concentration for semiconductors at the thermal equilibrium[36]

Furthermore, the dopant atoms may create extra dangling bonds in the structure which the increase in the doping level may lead to an increase of this bonds.

Finally, the doping efficiency in a-Si structure has some difficulties as Spear et al. measured the dark conductivity and activation energy for the both n-type and p-type doped a-Si versus their doping level. They demonstrate that after reaching a specific doping level, doping is saturated. There is a maximum level of dark conductivity that can be reached for p-type (10^{-2} $(\Omega cm)^{-1}$) and n-type(10^{-1} $(\Omega cm)^{-1}$) it is not possible to reach conductivity higher than these values [13]. They mentioned that from the obtained data, in a-Si it is not possible to push the fermi level more than half of the optical mid gap to the band edges (E_c and E_v)[20] [37].

As it is known, B doping in the a-Si has lower efficiency rather than c-Si which can be explained by structural differences. B atoms within the crystalline structure forms the fourfold configuration within the structure which inject mobile hole carriers and modify the fermi energy level and act as an active dopant. However, B configuration within the random network of the a-Si structure may not be the fourfold configuration. There are various assumptions regarding explaining the reason. One can be due to the B make a threefold configuration which make it inert and non-active dopant[35]. Another explanation is that the localized states within the conduction and valance band tails are related to the dangling bonds which increase the non-active dopants. Moreover, other studies showed that existence of H in the structure increases the probability of B atoms to get passivated and become inactive[38].

Huran et al. investigated the properties of a-SiC(N) deposited by introducing Ammonia (NH_3) precursor during the PECVD deposition of a-SiC. They varied the NH_3 flow rate from 0 to 12 sccm and then the electrical and optical properties are measured. For electrical characteristic measurement the Schottky barrier diode is prepared on SiC/Si as shown in Figure 1.8.

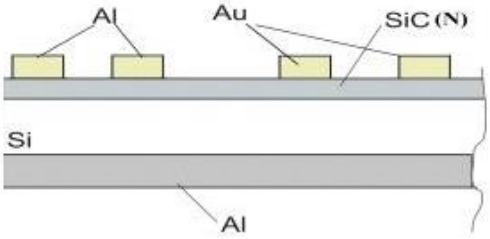

Figure 1.8. Cross section of Schottky barrier formed with Au and Al [39]

By measuring the reverse and forward I-V characterization, they have observed that by increasing the Ammonia gas flow rate the conductivity increases. From FTIR measurement, peaks according to CH_4 and SiH_4 precursors observed showing that the precursors are not decomposed completely by the plasma. They have concluded that the electrical conductivity of the samples with high Nitrogen content is higher than ones without any or small Nitrogen content[39].

1.3.5. Electrical behavior

The electrical and structural properties are dependent on the deposition conditions such as source gases, substrate temperature, and RF power. As it is mentioned before, by introducing C into the a-Si, disordering within the structure increases which affects the optical and electrical characteristics. By increasing the C, the optical band gap increases, however, the electrical conductivity of the thin film decrease since the band structure deviates more from, he expected crystalline structure.

Inoue et al. has achieved optical band gap of 2 eV for p-type a-SiC:H with dark conductivity of 3×10^{-7} $(\Omega cm)^{-1}$ prepared by photochemical vapor deposition. They have used C_2H_2 and dimethyl silane (Si $(CH_3)_2H_2$) precursors for C content. Higher dark conductivity is achieved when using $Si(CH_3)_2H_2$ precursor used compared to C_2H_2, which make it suitable for the window layer of the pin a-Si solar cells. Doping ratio effect on the conductivity measurements are also studied by them. They showed that optical band gap decreased by increasing the B_2H_6 concentration[40].

1.3.6. Optical properties

In optical and electrical applications of the SiC, it is preferred that the conductivity of the thin film is good enough and has a wide and tunable optical band gap (thin-film diode and thin-film solar cell)[41] . Amorphous and nano crystalline structures have advantages over the crystalline SiC. Lower deposition temperature, lower fabrication cost, and easy integration into the large area panels are some of the advantages. C incorporation inside the amorphous network depends on deposition condition such as precursor gas flow rates, RF power, deposition temperature, and post deposition treatments[42]. Bonding configuration of the Si and C atoms changes the optical and electrical properties. It has been observed that the optical band gap of the thin film increases as the RF power and substrate temperature increase[16]. As it is mentioned before, since the CH_4 molecule needs higher energy for decomposition, increasing the energy by increasing the RF-power and deposition temperature will provide enough energy.

Gandia et al. obtained high quality p-type window layer by RF glow discharge of a gas mixture of SiH_4. They investigated different RF power densities to reach better C incorporation in Two sets of A and B. in addition in other two sets (C and D) they varied the doping ratio to see the effects of changing boron trifluoride which they obtain their best conductivity of 2×10^{-7} $(\Omega cm)^{-1}$. Their structure of desired solar cell is glass/TCO/p-i-n/metal. For increasing the light absorption in the p layer, the optical band gap increased. They have assumed that increasing the optical band gap and achieving low activation energy lead to higher built in potential at the interface which will enhance the open circuit voltage. In addition, good conductivity may reduce the series resistance of the device. They have used CH_4 as the C containing precursor and boron trifluoride (BF3) as the doping gas which they believed it has better doping efficiency than B_2H_6. They first investigate, influence of adding CH_4 to the precursor gases which they have observed that indirect optical band gap increases from 1.8 to 1.92 eV as the CH_4 flow rate increases also, the Si-C related peak at $770cm^{-1}$ in the FTIR spectroscopy shown the existence of C in the a-Si lattice. Then in the second

deposition set they observed the higher C incorporation into the lattice by increasing the RF power density for the same CH_4 flow rate as the first set. However, the conductivity and doping efficiency got worse by increasing the C content which can be due to the increase in the disorder of the a-Si network. The results from these two sets showed that the low RF density for the same CH_4 flow rate improves the optical property.

Next, they have investigated the doping effect in both high and low power densities. For high RF power density as the doping increases, optical band gap decreases from 2.3 to 2.1 eV. However, the quality of the film decreases. For doping concentration around 10%, the maximum conductivity and low activation energy is achieved. For the fourth set they used the low RF power density as the previous sets. The low RF-power density should be high enough to be able to decompose the precursor gases and

Myong et al. investigated the effect of double p-type a-SiC:H layer in the p-i-n a-Si based solar cell. The p-type layer consisted of undiluted p-a-SiC:H as the window layer and a H_2 diluted p-a-SiC:H as the buffer layer. Improved doping efficiency of the B doped buffer layer decreased the recombination in the layer and at the interfaces. The window layers are deposited by photo assisted Chemical Vapor Deposition with C_2H_4, Si_2H_6, H_2, and B_2H_6 precursor gases. H_2 dilution improves the surface defects by decreasing the dangling bonds. However, they have observed that due to the relatively high amount of H creates bindings with B atoms[43].

CHAPTER 2

EXPERIMENTAL METHODS

In this chapter, the fabrication process is explained briefly. The sample preparation is the first step for this study which is followed by the deposition method. Following that the characterization techniques are explained.

2.1. Sample Preparation

In the thesis study, three substrates namely: 1) n-type double side polished float zone (FZ) monocrystalline silicon, 2) 1 µm thick silicon oxide (SiO_2) deposited on monocrystalline Silicon 3) 1.1 mm thick borosilicate glass have been used in every deposition, each aiming a different characterization technique as it is shown in Fig 2.1.

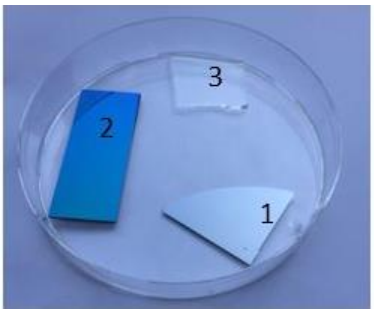

Figure 2.1. Substrates 1) n-type double side polished float zone (FZ) monocrystalline silicon, 2) 1 µm thick silicon oxide (SiO_2) deposited on monocrystalline silicon 3) 1.1 mm thick borosilicate glass

For solar cell fabrication, n-type double side polished FZ crystalline silicon wafers are used with 200 µm thickness and 1-3 Ω.cm resistivity. Wafers go through a chemical cleaning processes to clean both organic and in-organic contaminations. For cleaning processes, the wafers are dipped in four chemical cleaning agent as following:

The first, wafers are soaked in RCA1 bath (prepared with 5-parts water (H_2O), 1-part Ammonium Hydroxide (NH_4OH) and 1-part Hydrogen Peroxide(H_2O_2)) at 70˚C for

10 minutes then, rinsed with de-ionized (DI) water to obtain chemical free surface[44]. The Si surface was oxidized and chemical oxide was removed by HF:HCl:H_2O_2 solution just before next surface cleaning. The second, wafers are placed in RCA2 bath (containing 6-parts H_2O, 1-part H_2O_2 and 1-part Hydrogen Chloride acid (HCl)) at 70˚C for 10 minutes, and then, rinsed in DI water [44]. Afterwards, the wafers are soaked in a 5% hydrofluoric acid (HF) solution for 1 minutes then, dipped in Piranha solution (containing 3-parts sulfuric acid (H_2SO_4) and 1-part hydrogen peroxide (H_2O_2)) for 10 minutes[44]. Finally, samples rinsed in the DI water to remove all remaining chemicals from surface of samples. A layer of oxide covers the surface of wafers, which preserves them from the contaminations.

The crystalline silicon wafers are cut into small pieces (~2-3 cm) for the next process. Right before the deposition, in order to remove the chemical oxide over the silicon substrate, the silicon substrate is dipped in HF:HCl:H_2O (1:1:20) and then, rinsed in DI water. All the 3 substrates are placed on a holder to be co-deposited in the PECVD.

2.1.1. Plasma Enhanced Chemical Vapor Deposition (PECVD)

Chemical Vapor Deposition (CVD) is a technique to deposit thin films from gas precursors on the specified substrate by breaking the molecular bonds and rearranging the bindings with the help of high temperature. High temperature deposition has some drawbacks since it can negatively affect the dangling bonds passivation quality of intrinsic amorphous silicon thin film. Hence, in the industrial PV applications, using other means of supplied energy such as using plasma together with the low temperature deposition is prevailing.

GünEr Cluster PECVD system produced by VakSis which is placed at GUNAM cleanroom (Gunes enerji ve arastirma merkezi) has capacitively coupled plasma (CCP), inductively coupled plasma(ICP), sputtering system with two targets, load lock (LL), and transfer chambers enabling the system to deposit a-Si, micro crystalline silicon (µc-Si), and nanocrystalline silicon (nc-Si) thin films. Doping is a crucial step in the thin film deposition processes. In the PECVD system, the doping is an in-situ

process so, to eliminate the possible contamination during deposition from side walls of chambers, there are three different chambers in our system for each doping type (p-type and n-type) and intrinsic thin film. Thin film deposition in this work is done in the p-type CCP chamber.

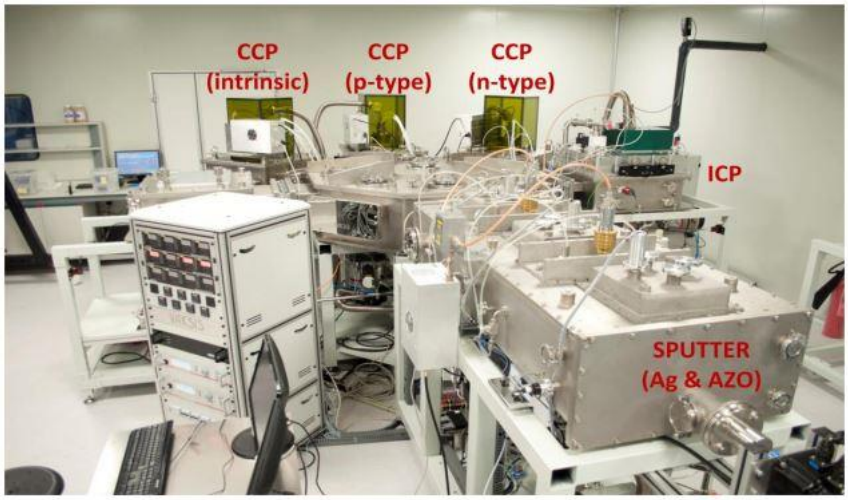

Figure 2.2. GünEr Cluster PECVD system [45]

The CCP chamber is made of two parallel metal plates (electrode) placed in a small distance within a reactor. The excitation power is a radio frequency (RF) power which operates at 13.56 MHz. One of the electrodes (cathode) is connected to the power supply and the other one (anode) is grounded. The temperature of the two electrodes can be controlled individually therefore, the temperature of substrate inside the chamber is more accurate. In this work, temperatures of the anode and cathode electrodes are set to 200 ˚C.

For each chamber, the gas precursors are supplied by gas lines connected to them. The flow rate of gas precursors mass flow rate is controlled by using MFC (mass flow controller), which controls the deposition conditions. The gas precursors enter the chamber through the shower head connected to the cathode leading to a uniform thin film deposition.

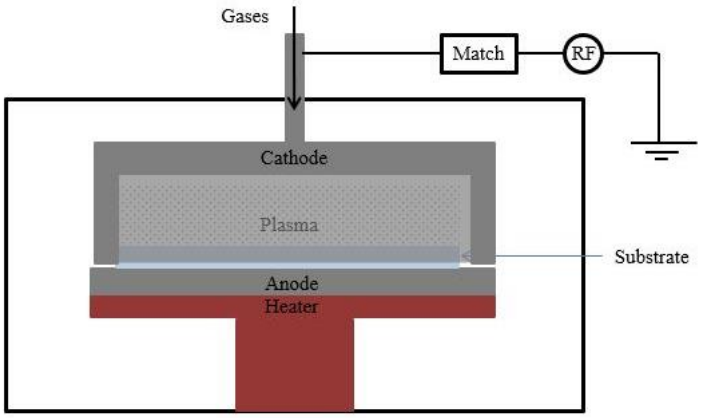

Figure 2.3. Schematic of the p type CCP chamber *[44]*

An electric field applied between two electrodes breaks the gas precursor molecules producing free electrons and ions mostly free-reactive radicals. These particles are accelerated by RF field and create charged particles by collision into the gas molecules [45][46]. The resultant particles rearrange in a new composition and lead to layer deposition.

In deposition process, the three substrates are placed on a holder in LL chamber. Then, the holder is sent to the p-type chamber where the heaters of the chamber are set to 200 ˚C and vacuum level is around 10^{-6} Torr. After placing the holder on the anode electrode in the chamber, the temperature stabilization in the chamber is done by the help of H_2 gas flow for 5 minutes. This step helps the substrates to be heated faster and to have uniform heat distribution through the holder. Then, the precursor gasses are set to desired flow rates for 3 minutes. In this duration, the gases are being mixed inside the chamber. The deposition starts by turning the RF plasma power on and stops when the RF power is turned off. It is better to wait for one minute to let the samples cool down slowly before taking them from the chamber. Then, the holder is sent to the LL chamber.

2.2. Characterization Techniques

For the optical and electrical characterization of the thin film, dark conductivity, temperature dependent dark conductivity and UV-VIS transmittance are carried out.

For measuring the dark conductivity, sample preparation including the metallization and annealing processes are explained. Afterwards, the measurement setup and the mathematical formulation are explained briefly. Moreover, temperature dependent conductivity and UV-VIS transmittance measurements, sample preparation and data analysis are given. In continue, X-ray Photoelectron Spectroscopy (XPS) measurement, Fourier Transform Infrared (FTIR) Spectroscopy and Spectroscopic Ellipsometry are explained.

2.2.1. Dark Conductivity

2.2.1.1. Sample Preparation

In order to perform this measurement, amorphous thin film is needed to be deposited on a nonconductive substrate covered by ohmic contacts.

For this measurement, the glass is used as the substrate for primary trials. The contaminations coming from the substrate hamper the electrical characteristics. Another option for choosing as the substrate is thick SiO_2 (1-micron) layer deposited on top of c-Si wafer. In addition, to prevent the interruption of the current path and the transport mechanism of electrons as well as making sure that there will be no electrical contribution from the c-Si substrate, we use sufficiently thick SiO_2 layer. B doped a-Si and B doped a-SiC are deposited on the substrate by PECVD.

Next step, Aluminum (Al) is deposited by thermal evaporation system on the samples in order to make an ohmic contact. The schematic of the thermal evaporation is shown below. Pure Al wires are placed on the resistive boat filament inside of the chamber and it is vacuumed around 10^{-5} torr. Electrical power heats up the filament and Al evaporates and deposits on the samples. Nearly 300 nm thick metal contacts are deposited on the samples [44].

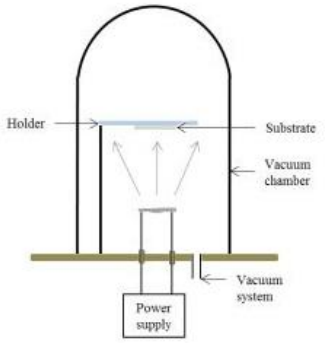

Figure 2.4. Thermal evaporation System[44]

A mask with the pattern of desired contacts has a rectangular shape with 1 cm length and 1 mm space between each contact as shown in Figure 2.5.

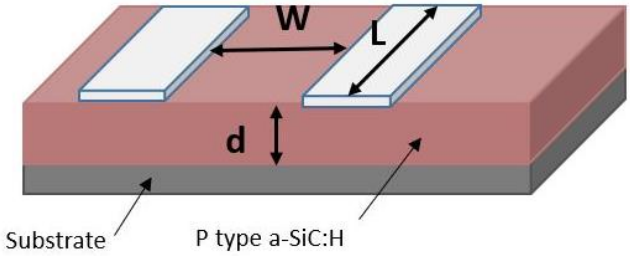

Figure 2.5. Experimental structure for conductivity measurements

2.2.1.2. Annealing Process

For measuring dark conductivity, annealing process after Al deposition is a crucial step in order to achieve the ohmic contact. For annealing process, furnace has been used. From the literature, it has been indicated that annealing at 180 ˚C for one and half an hour is enough to achieve the ohmic contacts [20] In order to optimize the annealing process, we take into account two boundary temperatures , one obtained from the literature and the other one is based on our deposition process temperature which alters between 200 ˚C and 250 ˚C. Since we do not want to exceed the deposition temperature in the annealing process, temperatures of 180 ˚C and 200 ˚C are chosen as annealing temperatures. Then, we investigate the dependency of the film

resistivity on the duration of the annealing process. We perform 3 steps of 30 minutes annealing, and after each step, we measure the conductivity of each sample.

2.2.1.3. Dark Conductivity Measurement

By applying the voltage on the two ohmic contacts and measuring the current, we can extract the dark conductivity. The measured current (I) is

$$I = A \times J \quad \text{(Eq.2.1)}$$

in which A is the cross-section of the film that the current is flowing, and J is current density.

The electric field is

$$E = V/W \quad \text{(Eq.2.2)}$$

in which V is applied voltage and W is distance between two electrodes.

For simplicity of the measurement, we assume that the current flows uniformly through the cross-section which is the product of thickness of the film (d) with the length of the ohmic contacts (l). By considering that the film is uniform, the carriers' density will be uniform through the layer [20]. Finally, the conductivity can be calculated as follows:

$$J = \sigma E \quad \text{(Eq.2.3)}$$

$$J = \left(q\mu_n n + q\mu_p p\right)E \quad \text{(Eq.2.4)}$$

$$\sigma = \frac{J}{E} = \frac{\frac{I}{d}l}{\frac{V}{W}} = \frac{I}{V}.\frac{W}{dl} \quad \text{(Eq.2.5)}$$

2.2.2. Temperature Dependent Dark Conductivity

The dark conductivity is dependent on the temperature in Kelvin as it is denoted in the Eqn. 2.6. This equation is for temperatures above the room temperature while the equation for temperature below the room temperature is not our case.

$$\sigma = \sigma_{\circ}\exp\left[-\frac{E_{act}}{K_B T}\right] \quad \text{(Eq.2.6)}$$

Which $\sigma_{\circ}$ named as conductivity prefactor(the minimum metallic conductivity by Mott) and E_{act} as activation energy [20].

It is worth mentioning that the dark conductivity for temperatures below the room temperature is dominant with the hopping between the nearest neighbors and localized states[47].

The samples of this measurement are prepared by gluing a wire contact on top of the deposited contacts to connect them to the cryostat. The samples are placed in the shielded cryostat (which thermally isolated) as it is shown in the Figure 2.6.

Figure 2.6. Shielded cryostat with sample placed on the electrode

In the cryostat, the liquid helium is used for cooling down and a heater for warming it up to the desired temperatures. The samples are placed on a metal electrode with the help of thermal paste which is thermally conductive. The cryostat first is vacuumed to 10^{-3} Torr and then cooled down by liquid helium. Then, the temperature is increased by 10 K steps from 50 to 350 K. For each temperature step, 1 to 2 minutes is required for temperature to be stabilized and then, the current density is measured by changing the voltage.

To obtain activation energy, the dark conductivity needs to be calculated for each temperature. Thus, from the ohmic region of the IV spectrum, the conductivity is calculated for each temperature. Then, the activation energy can be calculated for the

samples by plotting Arrhenius plot (natural logarithm of the dark conductivity multiplied by k_BT versus one over temperature) and linear fit to the linear part of plot, E_{act} can be obtained by slope of this function.

$$\ln(\sigma_d(T)) = \ln(\sigma_0) - \frac{E_{act}}{k_B T} \quad \text{[48](Eq.2.7)}$$

2.2.3. X-ray Photoelectron Spectroscopy (XPS)

The XPS measurement is used to identify the elements within the thin film structure and also provides information about the atomic concentration as well. In addition, extra information about the chemical bonding of the existed elements can be extracted which helps to analyze the C effects in the carbide formation. The schematic of the XPS setup is shown in the Figure 2.7. The surface of the sample is bombarded with X-rays and activate the photoelectron emission. Then the detector detects the emitted photoelectrons and their kinetic energies as well as their numbers. The emitted photoelectrons preserve the energy characteristics of the atoms. The elements detect by their own specific binding energies and the intensity of the binding energy is used for the element quantity determination. Since any bond configuration of the elements causes a shift in the binding energy so this make it possible for XPS to detect. This shift in the binding energies are because of the coulombic interaction between the core electrons of the elements. The XPS spectrum is made of different peaks for different bonds which can be deconvolved to detect each spectrum of bonds. First the XPS spectrum is corrected by shifting the Silicon peak in the spectrum to its value of 99.3 eV that is known as the Si-Si binding energy in Si element[49], then the whole spectrums are shifted as well. In addition, the spectrum of C1s, Si2p,and B1s are investigated to detect the peaks related to different bindings.

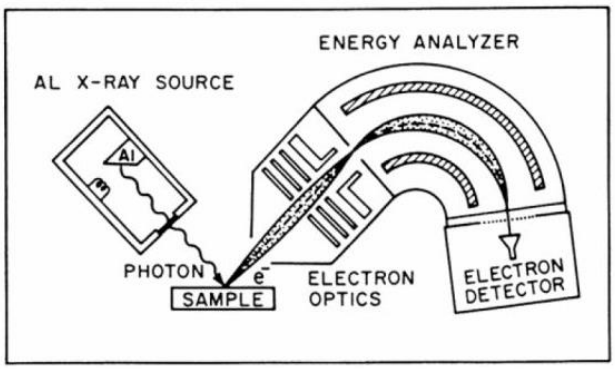

Figure 2.7. Basic XPS setup with X-Ray source to make photoelectron emission and an electron detector *[50]*

The binding energy ranges for different bonds are tabled below. Comprehensive list of bonds from the literature presented in chapter 3.

Table 2.1. *Binding energies for different bonds* [19]

Bonds	*Si-Si/Si-H*	*Si-C*	*C-Si*	*C-C/C-H*
Binding energy (eV)	99.2±0.1	100.5±0.1	283.4	286.4±0.1

Samples are cut into 5 mm^2 pieces. The samples first measured without removing the surface oxide and then the contamination and oxide of surface can be removed by sputtering. The PHI 5000 Versa probe XPS device with Al Kα X-ray source is used to measure the chemical bonds.

2.2.4. Fourier Transform Infrared (FTIR) Spectrophotometer

The chemical bonding and molecular structure can be investigated by FTIR spectroscopy. The vibrational modes of the molecules usually are happened to lie in the infrared region. If the electric dipole momentum of the molecule changes during the vibration, the vibration mode is infrared active. The FTIR system consists of a continuous light source, beam splitter, moving mirror, and a fixed mirror. The intensity of the transmitted light through the sample over the intensity of the incident light gives the transmittance (T) spectrum of the sample. It is better to deposit the thin

film on a pure double-sided polished c-Si with high resistivity to block free carrier absorption. The IR absorption is carried out by Bruker Equinox 55.

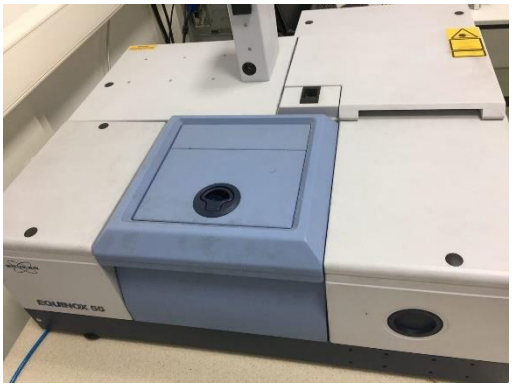

Figure 2.8. Bruker Equinox 55 FTIR

The spectrum is scanned between 400-4000 cm^{-1} wavenumber. The samples placed perpendicular to the infrared beam. The measurements take place at the room temperature and to achieve a better results Nitrogen (N_2) gas flow is used to purge the detector compartment. The scanning is done with 8 cm^{-1} resolution (slightly high resolution is chosen to decrease the artifacts such as fringes), aperture size (diameter) of 5 mm and scanner velocity of 10 kHz.

The absorbance (A) can be obtained from the transmittance using:

$$A = \log\left(\frac{1}{T}\right) \qquad \text{(Eq.2.8)}$$

Each time, absorbance spectra of bare Si are subtracted from the absorbance spectra of each sample in order to eliminate the effects of the substrate lattice. Since the carbon dioxide and water molecules exist in the atmosphere, they cause noise in the specific parts of the spectra. Therefore, these noisy parts are neglected from the spectra. To extract the peaks related to a specific chemical bonding, baseline correction is performed on the spectra. Then, a specific range of the spectrum is extracted for each chemical bond and baseline correction is performed again. Lorentzian and Gaussian functions are fitted to the corrected data and the peak value of each desired bond is obtained. The common chemical bonds and their wavenumbers a-SiC are mentioned

in the Table2.2 while, comprehensive vibrational from literature is mentioned in the chapter 3.

Table 2.2. *Common chemical bonds in the a-SiC and their vibrational wavenumber range*[19]

Chemical bonds	*Si-H*	*C-H*	*Si-H_n*	*B-H*
Wavenumber(cm^{-1})	600-650	760-770	2080	1400
	900,860	950-1110		
	2000	1250		
		1340		
		1400		
		2950		

From the IR absorption, information regarding the quantity of SiC and Hydrogen related bonds can be extracted. Analyzing the absorption spectra by deconvolving the peaks in the desired wavenumber ranges, with Gaussian and Lorentzian distributions.

The absorption coefficient can be extracted from the absorption spectra as below;

$$\alpha = 2.3\,\frac{A}{d} \qquad \text{(Eq.2.9)}$$

Which, A is the absorption spectra and d is the thickness of the thin film.

Hydrogen content is calculated by deconvolving the absorption spectra for Si-H bonds at 640 cm^{-1} as follows;

$$C_{H\approx\frac{A_w}{N_{Si}}\Sigma\nu/_w}\,\frac{\alpha(\nu)}{\nu} \qquad \text{[32](Eq.2.10)}$$

Which ν is the wavenumber of the absorption peak and ν_w represent the wavenumbers of the rocking-wagging bands, $A_w=1.6\times10^{19}$ $cm^{-2}$is the proportionality constant, the atomic density of pure Silicon is $N_{Si}=5\times10^{22}cm^{-3}$. Meanwhile it has been reported that the atomic density of a-Si slightly increases from the pure Si[32].

2.2.5. UV-VIS Optical Transmission

For measuring the optical transmission, the thin films are deposited on 1.1 mm thick borosilicate glass. The measurement is done by PerkinElmer Lambda 45 UV/VIS spectrometer for the wavelengths between 300-1000 nm. The transmission results are corrected by the transmission of the glass substrate reference. Since the reflection of the a-SI is high, the samples are placed in the device in such a way that the light goes through the glass then the deposited thin film as shown in Figure 2.9.

Figure 2.9. Perkin Elmer Lambda spectrometer

The parasitic reflection at the glass/thin film interface is neglected due to its low contribution to the transmission. Then tauc plot will be ploted to determine the optical band gap of the samples. Plotting the absorption coefficient multiplied by photon energy versus the photon energy. The absorption spectra and absorption coefficient will be calculated according to the Eq.2.8 and Eq.2.9 respectively.Then, the calculated band gap is compared for different B doping ratios, CH_4 gas flow rates, and H_2 gas flow rates. As it was mentioned in the introduction, the a-Si is direct band gap while adding C dopant to the structure makes it indirect band gap.

2.2.6. Spectroscopic Ellipsometry (SE) Measurement

Spectroscopic ellipsometry measurement is a well-known method which is used to indirect determination of not only optical properties of the thin films such as refractive

index and band gap of samples but also electrical properties of such thin films. By measuring dielectric properties of the sample also, thickness of samples is determined by this method. As it is shown in the figure below a polarized light is sent to the sample and the reflected back light is measured. The changes in the polarization of the light is used to determine the elliptic properties of the sample. To analyze the data Modified Forouhi-Bloomer model is used to fit the data. For fitting, a primitive guess of the thickness and band gap is needed.

The regression fitting continues until the fitting error (r^2) is around ~0.99. In this work, the band gap is calculated by both the ellipsometry and UV-transmittance. However, the band gap calculations by ellipsometry may differ from the UV transmittance results since there are some device limitation on how it measures the band gap.

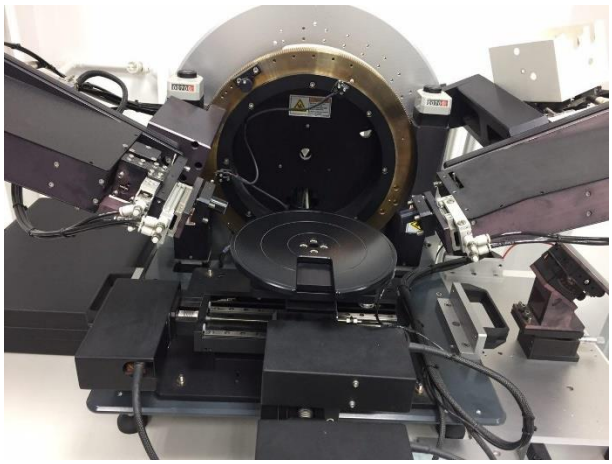

Figure 2.10. Ellipsometry device

CHAPTER 3

RESULTS AND DİSCUSSİONS

In this chapter, B doped a-Si:H and a-SiC:H deposition parameters and characterization results are explained and discussed in detail. The C incorporation into the structure and variable deposition parameters affect the optical and electrical properties of the amorphous structure. The RF power, CH_4, and H_2 gas flow ratios are varied to observe C incorporation. Moreover, from the best results of these experiments, the B_2H_6 and SiH_4 flow rates varied in order to improve the active doping concentration to obtain better quality films. The optical bandgap tuning is investigated by UV-VIS transmittance and the chemical bindings are investigated with FTIR, Raman and XPS. The conductivity and the activation energy are investigated to see the effects of C incorporation in doping of a-Si.

3.1. Deposition and Characteristics

3.1.1. Deposition

The process temperature refers to the temperature of the heaters which are placed close to each electrode. So, the substrate temperature is in the range of the deposition temperature. In order to have more homogenous heating in the chamber, significant works have been devoted such as installing plasma box and second heater in the chamber. In the current study, there are two heaters placed close to each electrode. The temperature variation of the substrate is measured by the thermocouples glued on the holder. This measurement is done without plasma, so the process temperature may vary from the mentioned amounts. However, after the temperature is set to a specific amount the temperature is stabilized around this value.

The deposition temperature is kept around 200 °C similar to the De Wolf et al. study which demonstrated that the passivation quality of a-Si is better when the deposition

temperature is around 200 °C [51][24]. As it is known, an intrinsic amorphous layer must be deposited on the c-Si in order to passivate the heterojunction structure.

Preheating before the deposition is an important step since it provides a better heat transmission to the sample. Therefore, the preheating with H_2 gas for 5 minutes is done for each deposition step. Deposition duration is normally 7 minutes for most of the samples. The samples are required to be thick enough for characteristic measurements because the electrical and optical characteristics for the thin films below 20 nm are hard to measure.

The process gases are as follows: Hydrogen (H_2), Silane (SiH_4), Methane (CH_4) and Diborane (B_2H_6). The C source in PECVD is CH_4. After preheating, the precursor gases are fed into the chamber and stabilized for 3 minutes before deposition. The gas flow rate controls the deposition process. So, the variation in the flow rates of each gas is investigated in this work to determine how gas flow rate effects the thin film characteristics.

3.1.1.1. Annealing

The results from the dark conductivity measurements show that contaminations from the glass hampers the conductivity measurements. The picture of the thin film deposited on the both substrates are shown in Figure 3.1.

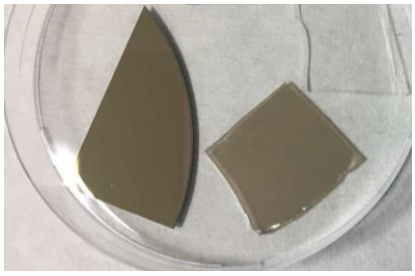

Figure 3.1. P-a-Si:H thin film deposited on SiO_2 and glass substrates:

In Table 3.1 Conductivity measurement results are shown for one of the p-a-Si:H samples. By comparing the conductivity measurements for both dark and under

illumination (AM 1.5 Global), SiO_2 substrate has been chosen as a substrate for this measurement instead of the glass.

Table 3.1.*Conductivity results for p-a-Si with glass and SiO_2 substrates*

Conductivity $(\sigma.cm)^{-1}$	*Glass substrate*	*SiO_2substrate*
Sample 42 dark	6.77×10^{-6}	2×10^{-5}
Sample 42 illumination	1.25×10^{-5}	3.35×10^{-5}

In case of annealing process optimization for the dark conductivity samples, two temperatures 180 °C and 200 °C are chosen considering the literature and deposition temperature as it is mentioned in the chapter 2. For the first set of samples, dark conductivity measurements showed that the films are poorly conductive. Then, we investigate the dependency of the film resistivity on the duration of the annealing process. We perform 3 steps of 30 minutes annealing, and after each step, we measure the conductivity of each sample. After the third step, we observe that the conductivity does not improve considerably as it is showed in the Table 3.2.

Table 3.2. *Annealing steps for optimization of annealing process for p-a-Si:H samples*

Conductivity $(\sigma.cm)^{-1}$	*Without annealing*	*Annealing at T=180 °C for 30 minutes*	*Annealing at T=200 °C for 30 minutes*	*Annealing at T=200 °C for 30 minutes*
p-a-Si:H 42	2×10^{-5}	7.9×10^{-5}	3.5×10^{-4}	5.4×10^{-4}

The optimized annealing temperature and duration for this measurement is 200 °C and 45 minutes respectively. The crystallization of a-Si is not the case of conductivity improvements because Si starts to crystallize around 550-600 °C. Also, in the case of c-Si, the deposition annealing after metallization should be around 500 °C in order to make a P^+ region at the interface to improve the resistivity of the contact.

3.2. Effect of RF-Power

In this work, all the RF (13.56 MHz) power mentioned are in Watt. The power density is calculated by dividing the power over the anode and cathode dimensions (30×30 cm^2). The importance of the power in this deposition method is that it provides the breakdown energy for different precursor gases with different binding energies. However, when power is increased, it leads to a more defective interface. Among the precursor gases, CH_4 and SiH_4 need higher energies for their molecular bonds to break. CH_4 has higher biding energy than SiH_4 so, it even needs higher energy than SiH_4 to decompose to active ions for the deposition [52]. In addition, at low RF power regime the energy is not sufficient to break the Methane molecules so the C-C bonds cannot happen[33].

To see the effects of changing the CH_4 gas flow rate on Carbide formation, the other precursors are kept constant. Based on our previous studies on p-a-Si:H, the flow rates of H_2, SiH_4, and B_2H_6 gases are kept at 120, 20, 30 sccm, respectively. Meanwhile, CH_4 gas flow rate is varied from 10 to 30 sccm.

As the RF power increases and the other deposition parameters are kept constant, it is expected to see that the increasing power will create more precursor radicals especially for CH_4. This can lead more C atoms to incorporate to the structure and the optical band gap increases. The power is set to 30,50, and 70 W.

3.2.1.1. Methane Gas Flow Rate at 10 sccm

Table 3.3 gives the deposition parameters of the first set. In order to observe the effect of power on the samples , all the deposition parameters are kept constant except power. For this set, CH_4 flow rate is 10 sccm. For the deposition at 70 W the deposition temperature started to increase after 2 minutes due to the chemical reaction in the chamber. The temperature is increased up to 280°C at the 4^{th} minute of the deposition thus, the deposition duration is 4 minutes for all samples at 70 W.

Table 3.3. *Deposition parameters for p-a-SiC:H with CH4 at 10 sccm for different powers*

Deposition parameters	*p-a-SiC:H-1*	*p-a-SiC:H-4*	*p-a-SiC:H-7*
Temperature(°C)	200	200	200
Pressure (Torr)	1	1	1
Deposition Duration (min)	7	7	4
SiH_4 flow rate (sccm)	20	20	20
B_2H_6 flow rate (sccm)	30	30	30
H_2 flow rate (sccm)	120	120	120
CH_4 flow rate (sccm)	10	10	10
Ratio $\frac{B_2H_6}{SiH_4}$	0.03	0.03	0.03
Ratio$\frac{CH_4}{CH_4+SiH_4}$	0.3	0.3	0.3
Power(W)	30	50	70

As it is mentioned above, the doping and CH_4 ratios are kept constant to see the effect of increasing power. The optical band gap and thickness of the samples are given in Table 3.4. Thickness of samples is measured by ellipsometry as it is explained in the chapter 2. As it can be seen, the thickness of the p-a-SiC:H-4 sample is nearly 60 nm thicker than p-a-SiC:H-1 because the power is increased from 30 to 50 W which means the deposition rate increases from 17.5 nm/min to 25.8 nm/min. Therefore, it can be assumed that the lower power does not provide enough energy to break the precursor in p-a-SiC:H-1 and that's why the deposition rate is lower. The XPS characteristics also are available for the C and Si atomic ratios and the C 1s and Si 2p spectrum of p-a-SiC:H-4 sample are shown in Table 3.5. However, the deposition duration is 4 minutes for p-a-SiC:H-7 sample, so, the thickness is expected to be lower than the other samples in this set. However, the optical band gap is higher comparing to the p-a-SiC:H-1 in this set.

Table 3.4. *Characteristic parameters for p-a-SiC:H with CH4 at 10 sccm for different powers*

Characteristics	*p-a-SiC:H-1*	*p-a-SiC:H-4*	*p-a-SiC:H-7*
Thickness(nm)	123	181	112
Band gap(eV) Tauc plot	1.60	1.83	1.79
Band gap(eV) ellipsometry	1.90	1.90	1.89

The optical band gap is calculated from the UV-VIS transmittance spectrum differs from the calculated band gap from the ellipsometry measurement. This difference in the calculated optical band gaps from different characteristic measurements also happened in the other studies as well [46]. This can be due to many reasons such as different growth mechanisms of the thin film on the glass and Si substrate and refractive indices of the thin film and the Si substrate is close to each other, makes it hard for the ellipsometry to measure the layers accurately [52]. Also, there are possible errors within measuring the transmittance during the UV-VIS transmittance measurement. Due to the explained divergences in the different measurement techniques, the optical band gap differs.

Tauc plot is illustrated in Figure 3.2 with a linear fitting function fitted to the linear part of the plot. The intersection of the fitted line and the X axis indicates the optical band gap of the sample. The optical band gap is also calculated from the ellipsometry results. In this study, the band gap is referred to the optical band gap calculated from the tauc plot.

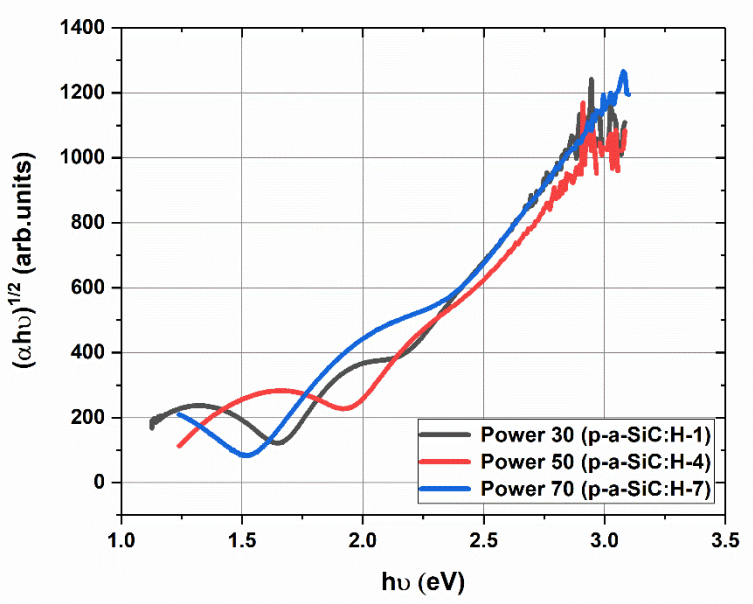

Figure 3.2. Tauc plot for p-a-SiC:H with CH_4 at 10 sccm for different powers

The Figure 3.3 shows the XPS results of C 1s for sample p-a-SiC:H-4. Then by comparing the results with the XPS data from the literature survey which are mentioned in the Appendix and Table 3.5, the results show that the C incorporation is not only dedicated to the specific bindings in the thin film. Also, it should be mentioned that the total atomic concentration does not contain H atomic concentration. Since H atomic concentration cannot be measured by XPS measurement, the given atomic concentrations do not demonstrate the real atomic concentrations within the sample.

Table *3.5. Atomic concentration from XPS measurement of p-a-SiC:H-4*

p-a-SiC:H-4	*C1s*	*Si2p*
No ion etching	25.18	74.81
After ion etching for 3 min	2.34	97.65

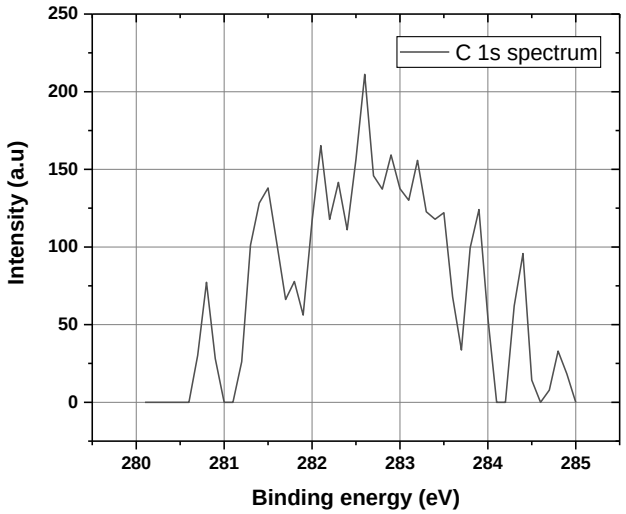

Figure 3.3. XPS results for C 1s for p-a-SiC:H-4

The H content can be determined from FTIR measurement by the method that is explained in the chapter 2. From analyzing the absorption spectra in 600-700 cm^{-1} and 1900-2100 cm^{-1} regions separately. The peaks are deconvolved by Gaussian and Lorentzian distributions at the desired peak positions. Related Si-H bindings are published in several works which are shown in Table 3.6.

The consistency of the H content in the structure of thin film in the two wavenumber regimes of Si-H (Si-H wagging-rocking around 640 cm^{-1} and Si-H stretching around 2000 cm^{-1}) and the precursor flow rates are also investigated [24].

Providing higher energy by increasing the power can lead to break more CH_4 molecules and provides more H into the structure of the B doped a-SiC:H and the optical band gap increases. It is stated in studies [24], that the Si rich thin film has a significant absorption up to 600-700 cm^{-1}. On the other hand, higher Si-H bonds leads to low Si-Si bonds and it is expected to see a less dense thin film as it is has higher deposition rate. The common chemical bonds existed in the a-SiC:H is extracted from different studies are tabulated below.

Table 3.6. *FTIR peak position from literature survey*

Bond	*Peak position wavenumber (cm^{-1})*	*Reference*
$C\text{-}H_n$ (Stretching)	2850 to 2960	[46]
Si-H(Stretching)	2000 to 2140	[46]
$Si\text{-}CH_n$	1250 to 1470	[46]
C-C	1300	[46]
$Si\text{-}CH_3$ or Oxygen	960	[46]
SiC	740-770	[46]
SiC	780	[53]
$SiC\text{-}H_3$	980	[53]
$Si\text{-}H_n$	2070-2100	[53]
$C\text{-}H_n$	2900	[53]
$Si\text{-}CH_3$	1250	[33]

As it mentioned in the literature, the C-C, C=C, C-H and Si-C bonds are involved in the increasing of optical band gap. As it is mentioned in the Table 3.6 the $C\text{-}H_n$ bonds lie in the 2900 cm^{-1} spectrum of the FTIR so it is kind of difficult with the possible molecules in the air and also the limitation of the detection of the spectrometer to detect them. Also, for the C-C and B-H bonds that their vibrational frequencies lie in the 1300- 1500 cm^{-1} range of the FTIR spectrum due to interference of the H_2O and CO_2 molecule's spectrum, it is hard to extract the desired bond related peaks.

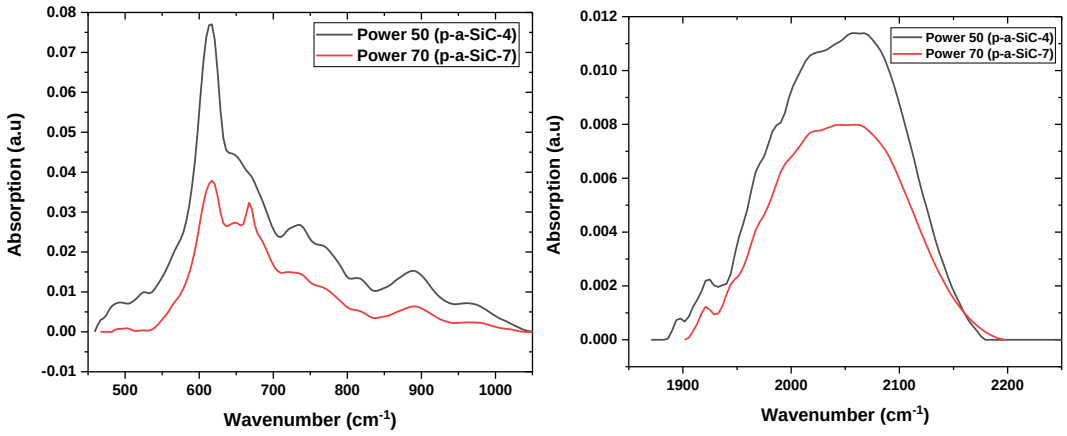

Figure 3.4. FTIR spectra for p-a-SiC:H with CH_4 at 10 sccm for different powers

Comparison of the FTIR spectra of first set which are shown in Figure 3.4, show that by increasing power the intensity of the Si-H bond peaks decreases, this may assist in explaining the decrease in optical band gap.

As it can be seen from Figure 3.5, the dark conductivity slightly improves as the power increases for the samples. Also, the samples become more photosensitive. It reveals that increasing power for the same CH_4 flow rate at 10 sccm helps to better incorporation of the dopant in the structure of the thin film.

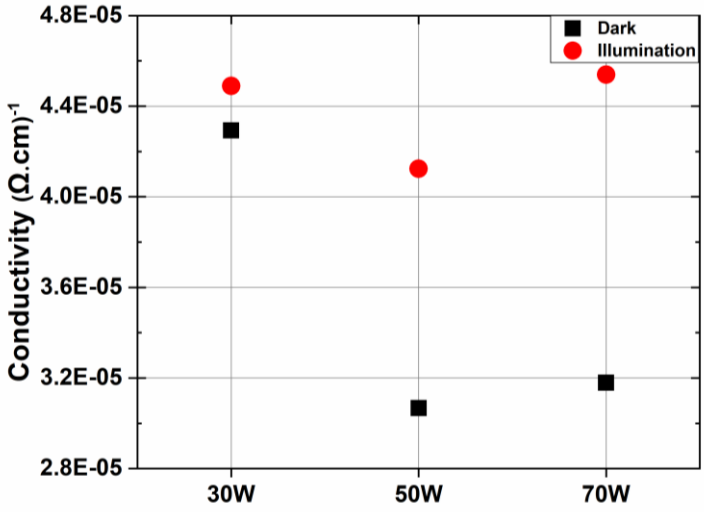

Figure 3.5. Conductivity of p-a-SiC samples with CH_4 at 10 sccm for different powers

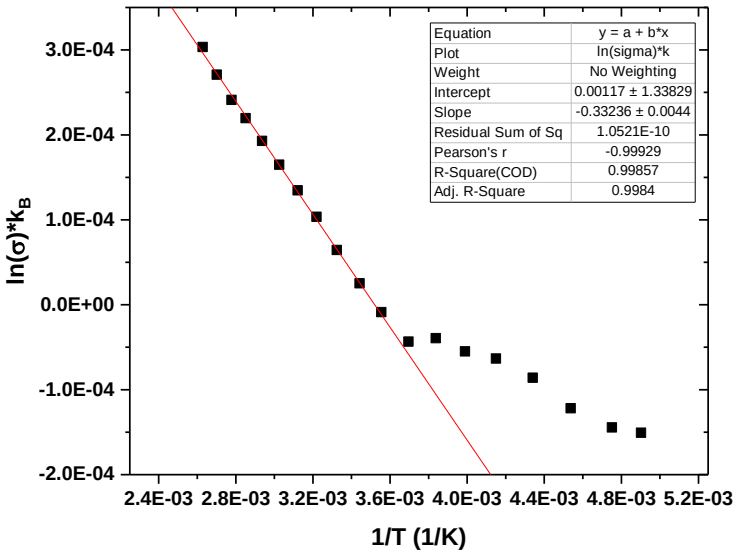

Figure 3.6. Arrhenius plot for p-a-SiC:H-7

Activation energy (E_{act}) for sample p-a-SiC:H-7 is measured by measuring the dark conductivity of sample for 50 to 350 K temperatures as it is explained in chapter 2. The activation energy is 0.33 eV. Zhang et al. demonstrates E_{act}=0.45 eV for p-a-Si samples and Heredia et. al reaches activation energy of 0.45eV for high B incorporation for their a-Si samples[54][55]. For this sample with optical band gap of 1.79 eV, the E_{act} lies in 0.33 eV distance from the Valence band as it is approximately shown in Figure 3.7. In order to simplify the band diagram of the a-SiC samples, the valance and conduction band edges are shown as valance and conduction band as same as c-Si and E_f is the fermi energy level.

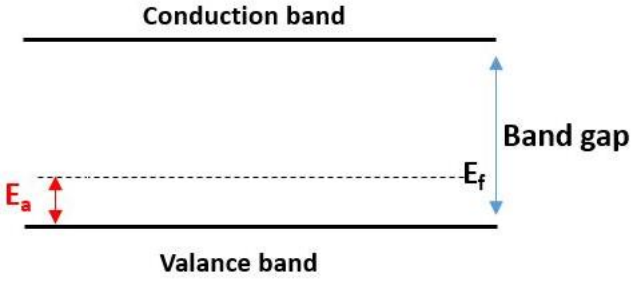

Figure 3.7. Band state diagram for p-a-SiC:H-7

3.2.1.2. Methane Gas Flow Rate at 20 sccm

In the second set which is tabulated in Table 3.7, the changes in the power shows the same trend as the first set. In this set, CH_4 gas flow rate increases up to 20 sccm. With increase in the CH_4 flow rate it is expected that the C and H incorporation in the thin film improve which could lead to higher optical band gap.

Table 3.7. Deposition parameters for p-a-SiC:H at CH_4 at 20 sccm for different powers

Deposition parameters	*p-a-SiC:H-2*	*p-a-SiC:H-5*	*p-a-SiC:H-8*
Temperature(°C)	200	200	200
Pressure (Torr)	1	1	1
Deposition Duration (min)	7	7	4
SiH_4 flow rate (sccm)	20	20	20
B_2H_6 flow rate (sccm)	30	30	30
H_2 flow rate (sccm)	120	120	120
CH_4 flow rate (sccm)	20	20	20
Ratio $\frac{B_2H_6}{SiH_4}$	0.03	0.03	0.03
Ratio$\frac{CH_4}{CH_4+SiH_4}$	0.5	0.5	0.5
Power(W)	30	50	70

The optical band gap is increased as the power increases which is indicated in Table 3.8. It is expected since more energy is provided for the precursor gases to break into active ions. Meanwhile, the optical band gap of the second set with CH_4 at 20 sccm is higher in comparison with the first set (the CH_4 gas flow rate is at 10 sccm). It can be due to the increasing CH_4 flow rate which provides more C and H into the structure.

Table 3.8. *Characteristic parameters for p-a-SiC:H with CH_4 at 20 sccm for different powers*

Characteristics	*p-a-SiC:H-2*	*p-a-SiC:H-5*	*p-a-SiC:H-8*
Thickness(nm)	120	181	114
Band gap(eV) Tauc plot	1.67	1.90	1.94
Band gap(eV) Ellipsometry	1.81	2.00	1.97

As the deposition power increases the deposition rate increases for this set as the same as the first set. The optical band gaps of the second set are calculated from the related tauc plots shown in Figure3.8.

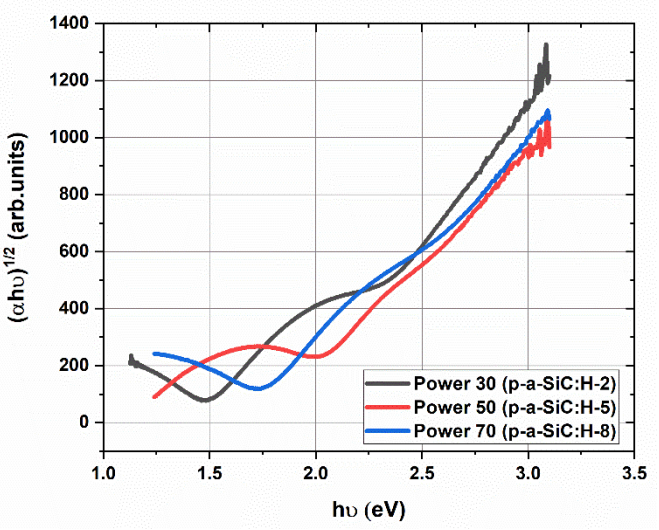

Figure 3.8. Tauc plot for p-a-SiC:H with CH_4 at 20 sccm for different powers

The conductivity results for the second set are shown in the Figure 3.9. As the optical band gap increases by increasing the power, the conductivity improves. The conductivity is not photosensitive. It can be linked to the B atoms in the a-SiC:H structure are not placed as interstitials. The FTIR spectrum is also measured as it is shown in Figure 3.10.

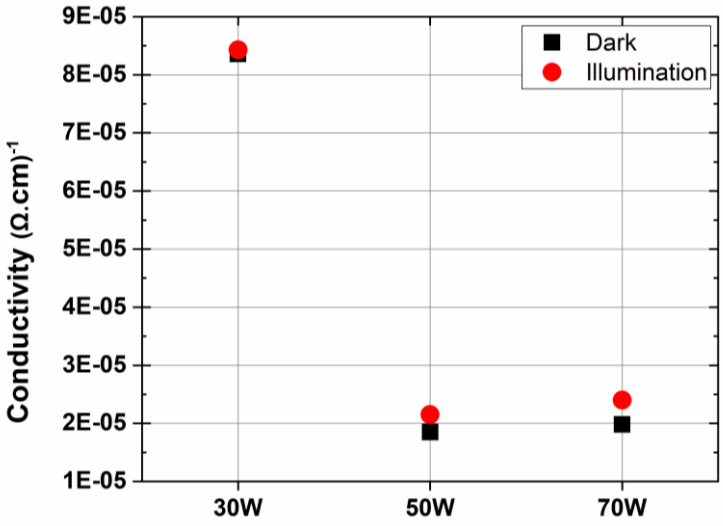

Figure 3.9. Conductivity of p-a-SiC:H sample for CH_4 at 20 sccm for different powers

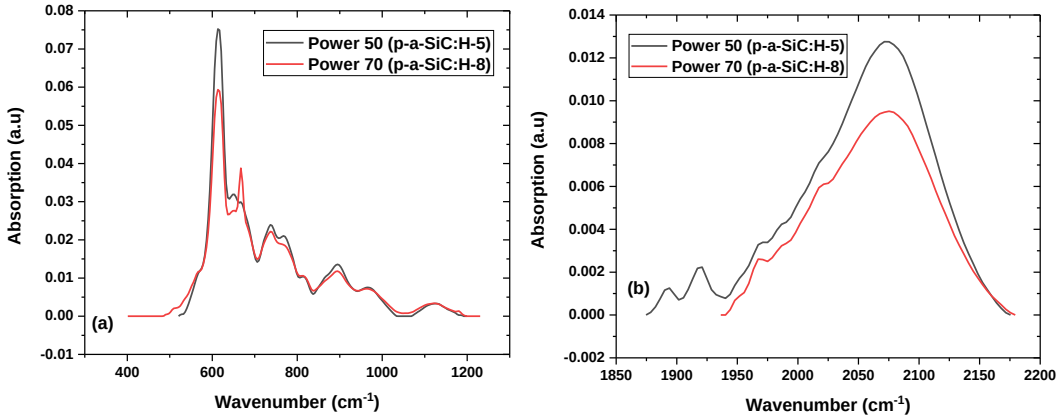

Figure 3.10. FTIR spectra for p-a-SiC:H with CH_4 at 20 sccm for different powers

By comparing the two FTIR spectrum of the sample p-a-SiC:H-5 and p-a-SiC:H-8 in the Figure 3.10 we can see that the intensity of the bonds is relatively higher for 50W power. Which indicate that the concentration of the related bonds is higher inside the structure. The peaks that we observe in the Figure 3.11 (a) and (b) for p-a-SiC:H-5 sample are as follows; Si-C stretching at 650cm^{-1}, Si-C wagging at 770 cm^{-}1, Si-H stretching peak at 2073 cm^{-1}, SiC-H_3 peak at 973 cm^{-1} . For p-a-SiC:H-8 the fitted spectrum is shown the (c) and (d) parts of Figure 3.11 some of the peaks are; Si-C stretching at 660cm^{-1},Si-C wagging at 770 cm^{-1}, Si-H stretching peak at 2074 cm^{-1},

SiC-H_3 peak at 975 cm^{-1} . In order to demonstrate the related peaks clearer, only some of the deconvolved peaks are plotted in the figures.

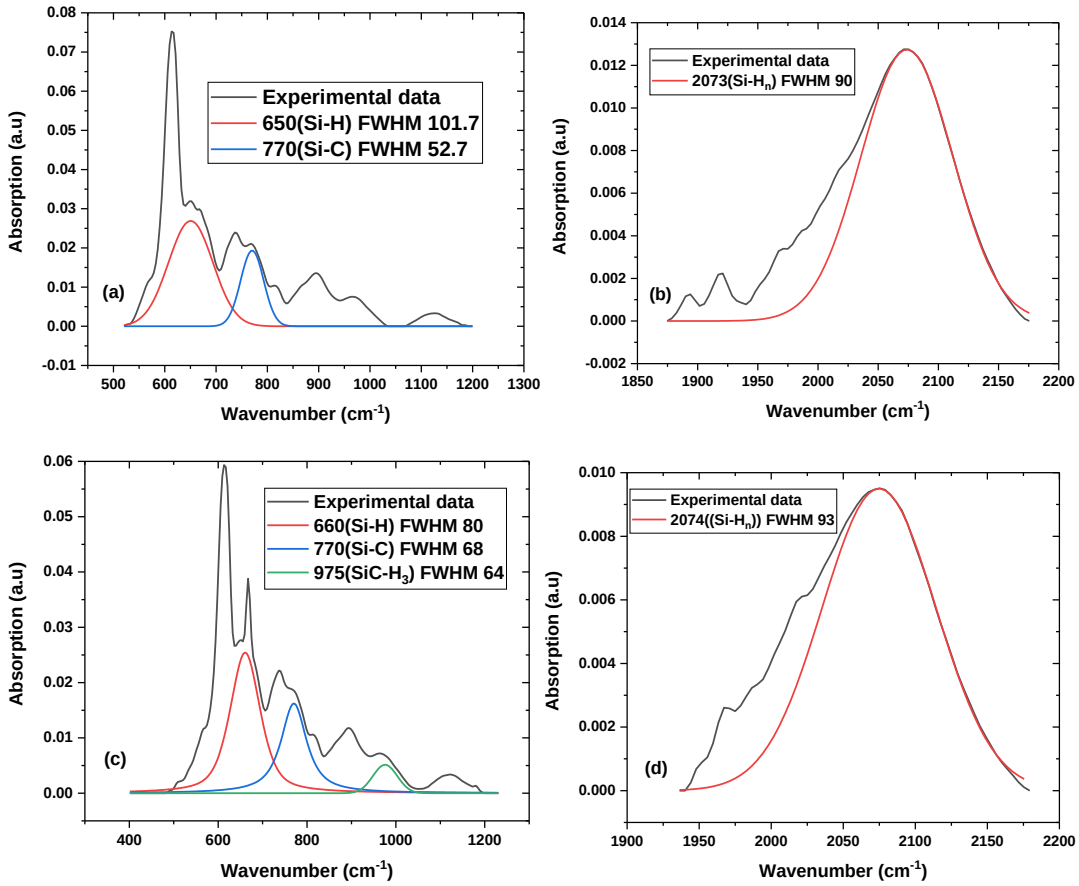

Figure 3.11. Detailed FTIR spectrum of a) b) p-aSiC:H-5 and c) d) p-aSiC:H-8

The atomic concentration for this set is tabulated in Table 3.9. Although the C and B incorporation is high for the sample p-a-SiC:H-2 is higher than the other samples in this set but the conductivity and optical band gap is lower. From the XPS results the C spectrum is investigated to get information about the structure network. The XPS results are shown in Figure 3.12. The peaks at 281.9 eV and 282.3 eV in the part a of the figure are referred to the alpha-SiC and Beta SiC structures[56][57]. It can also assume that in the short distance structure of the a-SiC:H which is detected by XPS has the same structure as Si. The Si-C bond at 283.6eV also exist but the intensity is low.

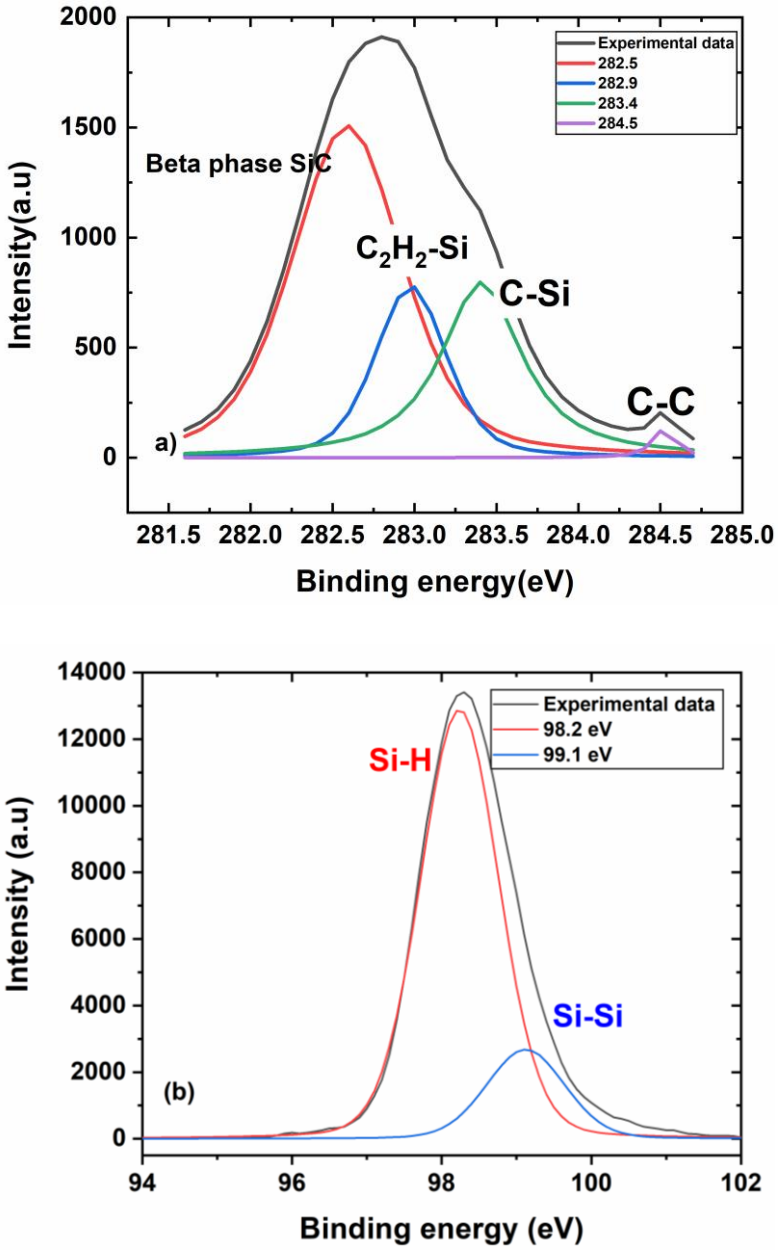

Figure 3.12. XPS spectrum of p-a-SiC:H-2 (a) C 1s (b) Si 2p

Figure 3.12 b) shows the binding of Si in the p-a-SiC:H-2 sample. Two peaks at 98.2 eV and 99.1 eV are related to the Si-H and Si-Si bonds in the structure, also the binding energy of Si-Si in this structure is close to binding energy of this bond in crystalline structure[58][59]. It can be deducted that although the atomic ratio of the C and B is higher than other samples in the second set, but the C is not bonded properly with Si.

It can be deducted that the incorporated C is bonded to H in the structure and the C-Si bond has low intensity.

Table 3.9. Atomic concentration from XPS measurement in the doped a-SiC:H samples

p-a-SiC:H-2	*C1s*	*Si2p*	*B1s*
No ion etching	29.54	64.86	5.59
After ion etching for 3 min	10.42	82.39	7.18
p-type a-SiC-5	*C1s*	*Si2p*	
No ion etching	26.27	73.72	
After ion etching for 3 min	2.58	97.41	
p-type a-SiC-8	*C1s*	*Si2p*	
No ion etching	17.48	82.52	
After ion etching for 3 min	1.33	98.67	

The binding energy of C-C and C-H bonds are close to each other, so it is hard to distinguish between them in the peak fitting. Also, the Si-Si and Si-H binding energies has small difference (nearly 0.1 eV), it is hard to deconvolve these peaks accurately and these peaks are shown as one peak in this study.

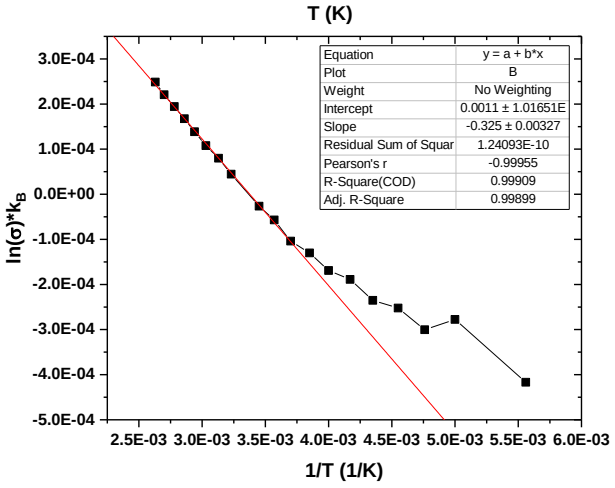

Figure 3.13. Arrhenius plot for p-a-SiC-5

The activation energy for p-a-SiC:H-5 is around 0.32 eV.

3.2.1.3. Methane Gas Flow Rate at 30 sccm

In this sample set, the CH_4 gas flow rate is 30 sccm.

Table 3.10. *Deposition parameters for p-a-SiC:H with CH4 at 30 sccm for different powers*

Deposition parameters	*p-a-SiC:H-3*	*p-a-SiC:H-6*	*p-a-SiC:H-9*
Temperature(°C)	200	200	200
Pressure (Torr)	1	1	1
Deposition Duration (min)	7	7	4
SiH_4 flow rate (sccm)	20	20	20
B_2H_6 flow rate (sccm)	30	30	30
H_2 flow rate (sccm)	120	120	120
CH_4 flow rate (sccm)	30	30	30
Ratio $\frac{B_2H_6}{SiH_4}$	0.03	0.03	0.03
Ratio$\frac{CH_4}{CH_4+SiH_4}$	0.6	0.6	0.6
Power(W)	30	50	70

As it is shown in the Table 3.11 the characteristic parameters for the third set is mentioned. The deposition rate for the CH_4 flow rate at 30 sccm increases as the power increases. However, for the three samples deposited at 50Watt among these three sets, the deposition rate for p-a-SiC:H-6 with CH_4 at 30 sccm is lower than CH_4 at 10 and 20 sccm (p-a-SiC:H-4 and p-a-SiC:H-5). This can be due to the high CH_4 ratio decomposition and the SiH_4 decomposition is less. Also, from the XPS Results for p-a-SiC:H-6 , the higher atomic ratios for C and B atoms inside the thin film and lower Si concentration can be observe. These parameters can assist in explaining the lower deposition rate.

Table 3.11. Characteristic parameters for p-a-SiC:H with CH_4 at 30 sccm for different powers

Characteristics	*p-a-SiC:H-3*	*p-a-SiC:H-6*	*p-a-SiC:H-9*
Thickness(nm)	110	142	114
Band gap(eV) Tauc plot	1.68	1.89	1.90
Band gap(eV) Ellipsometry	1.60	1.99	1.88

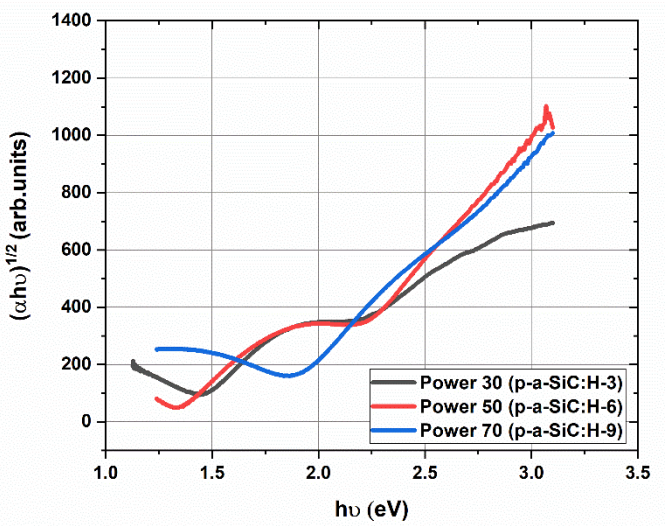

Figure 3.14. Tauc plots for p-a-SiC:H with CH_4 at 30 sccm for different powers

The optical band gap is increasing as the power increases which this trend is kind of same within these three sets so far.

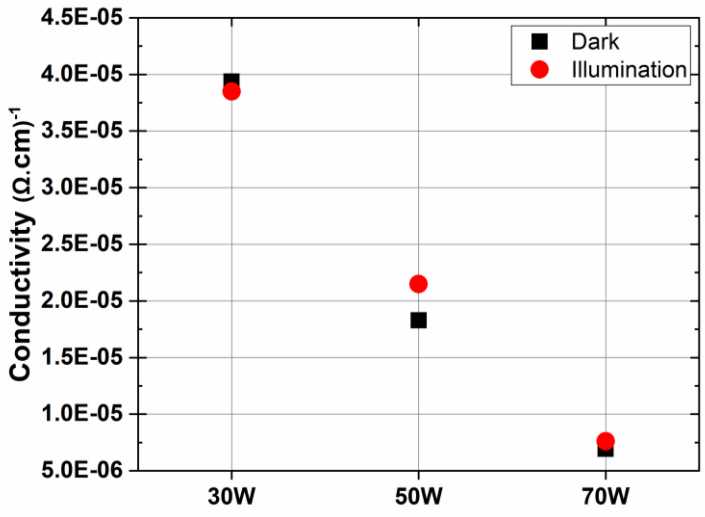

Figure 3.15. Conductivity of p-a-SiC:H sample for CH_4 at 30 sccm for different powers

The conductivity of this set (Figure 3.15) decreases as the optical band gap increases. For sample p-a-SiC:H-6, the conductivity is photosensitive which can be due to better B placement inside the amorphous structure. Also, the decrease of conductivity for sample p-a-SiC:H-6 can be deducted to higher C incorporation which can also act as defect states inside the network.

Table 3.12. *Atomic concentration from XPS measurement in the p-a-SiC:H-6*

p-a-SiC:H-6	*C1s*	*Si2p*	*B1s*
No ion etching	34.09	62.85	3.04
After ion etching for 3 min	16.10	77.80	6.09

The XPS measurement has limitation in measuring samples. If the atomic ratio is in range of 0.1 to 1 atomic percent, it is in the detection limitation range so it won't be detected properly. On the other hand, detecting B is hard since diffusivity of this atom in c-Si is low but it is slightly higher in case of a-Si. The B atom detection by XPS is limited. The individual spectrums of the XPS measurement for sample p-a-SiC:H-6 are shown in Fig 3.16.

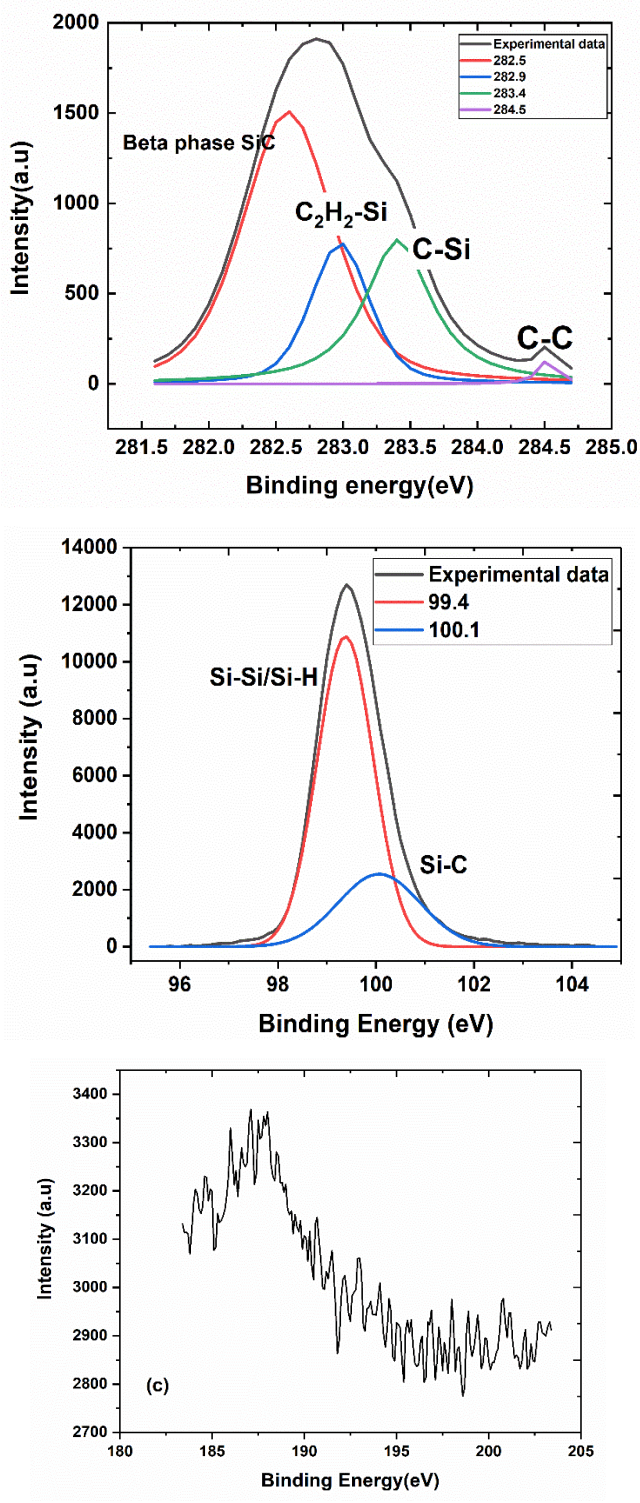

Figure 3.16. XPS results for p-a-SiC:H-6 a) C1s b) Si 2p C) B 1s

The FTIR data is shown in the Figure 3.17 for the third set. Spectrum of two samples depicted.

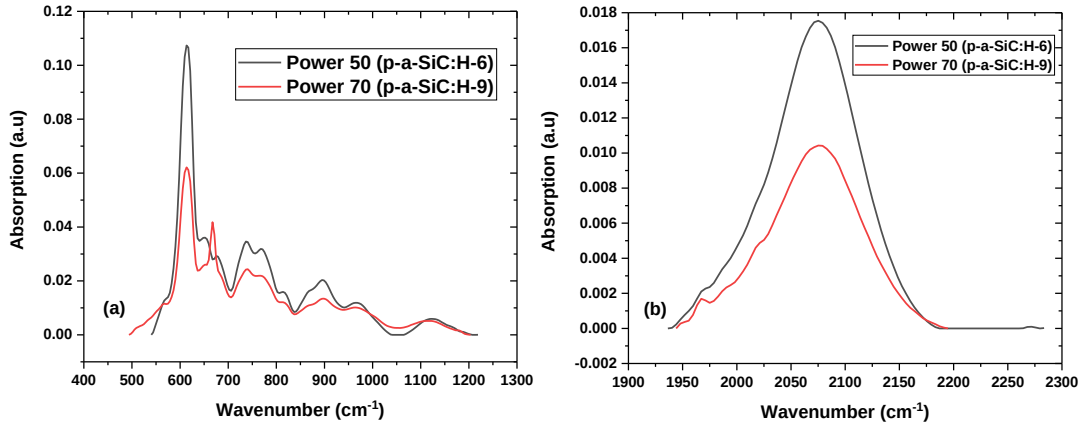

Figure 3.17. FTIR spectra for p-a-SiC:H with CH_4 at 30 sccm for different powers

Detailed spectrum of sample p-a-SiC:H-6 is depicted in Figure 3.18 (a) and (b). The Si-H wagging-rocking vibrational bond at 650 cm^{-1}, Si-C wagging at 774 cm^{-1}, Si-H stretching peak at 2075 cm^{-1}, SiC-H_3 peak at 967 cm^{-1}. Same bonds are also detected in the p-a-SiC:H-9 as well; Si-H wagging-rocking bond at 661cm^{-1}, Si-C wagging at 768 cm^{-1}, Si-H stretching peak at 2076 cm^{-1}, SiC-H_3 peak at 976 cm^{-1}. From Figure 3.18 (a) and (c) comparison it is clear that the absorption intensity of the Si-C bond is higher for p-a-SiC:H-6 as well as the Si-H bond concentration (wagging-rocking and stretching bonds together)which is also verified from the XPS data that the C incorporated in this sample is higher than p-a-SiC:H-9.

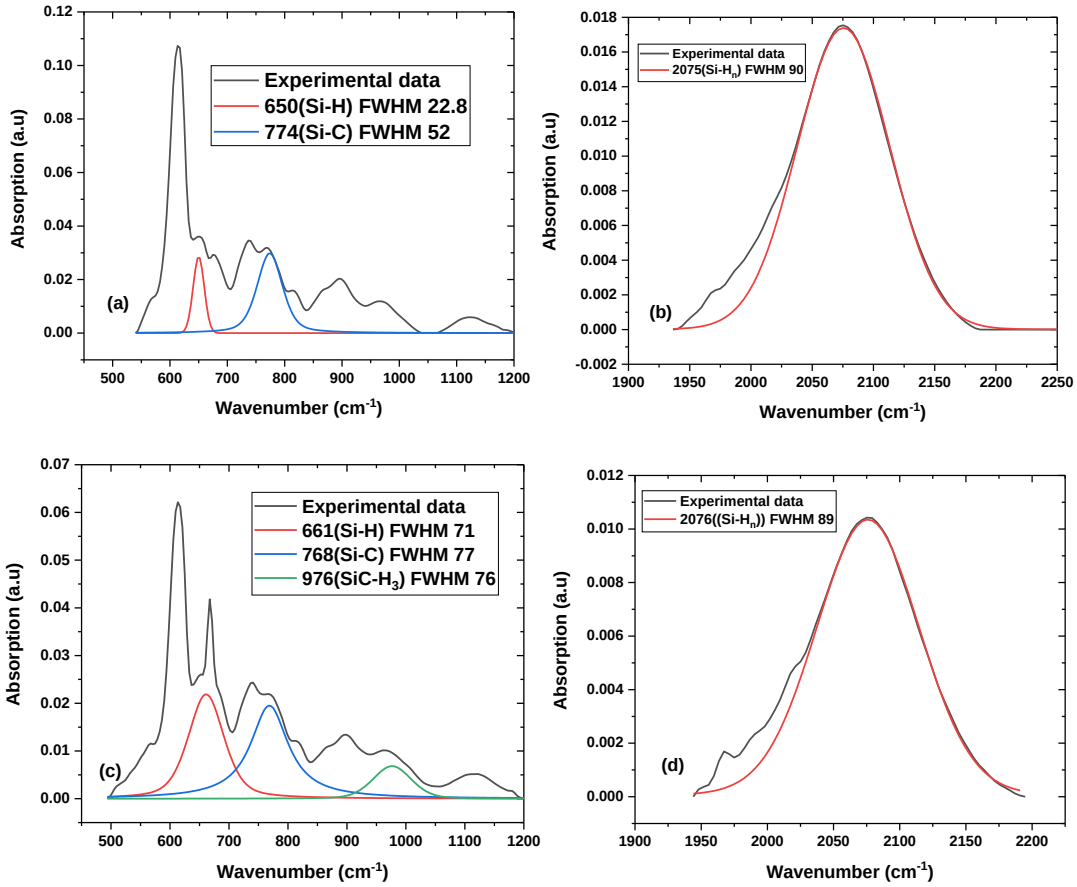

Figure 3.18. FTIR spectrum of sample p-a-SiC:H-6 (a) and (b) and sample p-a-SiC:H-9 (c) and (d)

Activation energy for p-a-SiC:H-6 is calculated from the Arrhenius plot in Figure3.19.

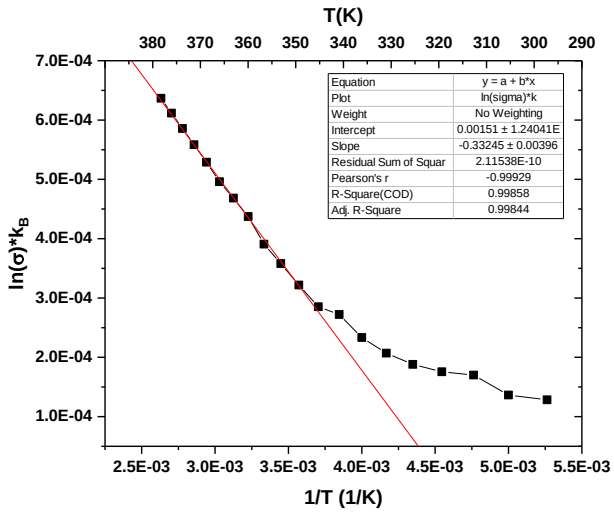

Figure 3.19. Arrhenius plot for p-a-SiC:H-6

The XPS measurements give us the chemical binding configuration of the thin film structure. The binding with different atoms shifts the binding energy of an element in a specific amount which helps us to detect the bond in the XPS. The reason for this shift is the coulombic interaction of the core electrons of the atoms which cause the shifting in the binding energy. For instance, the Si electrons in pure Si binding energy is 99.2 eV however, the Si electrons in the Si-C bond has binding energy 100.5 eV [19]. The XPS spectrum for an element consists of different bonds of the element so it can be deconvolved into the bonds. The Table 3.13, a list of Si related chemical bonds and their binding energy from different sources is listed. Table 3.14 contains XPS peaks related to B 1s from different studies. Table3.15 C1s peaks from literature survey are inserted.

Table 3.13. *Chemical bonds of Si 2p and their binding energy in different studies in literature*

Chemical bonding (Si 2p)	*Binding Energy (eV)*	*FWHM*	*Structure*
Si-C bond in tetrahedral SiC[27]	100.5	1.5	
Si bond to sp2 C-C/C-H[27]	101	1.8	
Si-C bond in tetrahedral SiC[27]	100.4	1.3	
Si-Si/Si-H[27]	99.7		
Si-Si[53]	99.2	2.13	HWCVD aSiC:H
Si-C[53]	100.5	1.38	HWCVD aSiC:H
O-Si-C[53]	101.8		HWCVD aSiC:H
SiO_x[53]	103.2		HWCVD aSiC:H
Si-Si [58]	99		Crystaline
Si-Si[59]	99.16		Crystalline p-doped

Table 3.14. *Chemical bonds of B 1s and their binding energy in different studies in literature*

Chemical bonding(B 1s)	*Binding Energy (eV)*	*FWHM*	*Structure*
β_r-B[60]	187.9		
β_r-B[60]	187.3		
B-B/B-Si [61]	186		B doped a-Si PECVD

Table 3.15. *Chemical bonds of C 1s and their binding energy in different studies in literature*

Chemical bonding (C 1s)	*Binding Energy (eV)*	*FWHM*	*Structure*
C-Si bond in tetrahedral SiC [27]	283.4	1.3	
Sp2 C-C/C-H bonds to Si [27]	284.6	1.5	
C-O-Si/C-Si-O bonds in oxycarbide [27]	285.6	1.2	
C-Si bond[28]	283.4		
C-Si bond[42]	283.5		RF Plasma Sputtered 400W,5Pa
C-Si bond[42]	280.75		RF Plasma Sputtered 200W,5Pa
C-Si [53]	283.2		HWCVD aSiC:H at C_2H_2 6 sccm
C-C[53]	284.6	2.1	HWCVD aSiC:H at C_2H_2 6 sccm
C-O-H[53]	286.4		HWCVD aSiC:H at C_2H_2 6 sccm
C=O[53]	288.4		HWCVD aSiC:H at C_2H_2 6 sccm
C-Si[19]	283.2		aSiC:H
C-C/C-H[19]	284.6		aSiC:H
C-O-H[19]	286.4		aSiC:H
C=O[19]	288.4		aSiC:H
C2H2/Si[62]	282.7		
C-Si[57]	281.45		Crystalline βphase
C-Si[56]	281.3		Crystalline αPhase

3.3. Effect of Hydrogen Flow rate Variation

In this set effects of decreasing the SiH_4 and B_2H_6 gas flow rates and increasing H_2 flow rates on SiC properties are studied in detail. It is expected to achieve an a-SiC alloy with a structural network more similar toward C-Si structure with creating SiH_4 starving situation[33]. It is well known that for a-Si based alloys as the alloy content increases the disorder in the structure increases which this will diminish the mobility of the carriers[33]. Pereyra et al. is studied the effects of SiH_4 starving plasma plus H_2 dilution in doping of a-SiC:H network. This will assist in interpreting the results of XPS measurement for this set.

Table 3.16. *Deposition parameters for p-a-SiC:H with CH_4 at 30 sccm for different H_2 flow rates*

Deposition parameters	*p-a-SiC:H-10*	*p- a-SiC:H-11*	*p- a-SiC:H-12*	*p- a-SiC:H-13*
Temperature(°C)	200-200	200-200	200-200	200-200
Pressure (Torr)	1	1	1	1
Deposition Duration (min)	5	5	5	5
SiH_4 flow rate (sccm)	11	11	11	11
B_2H_6 flow rate (sccm)	5	5	5	5
H_2 flow rate (sccm)	200	300	400	500
CH_4 flow rate (sccm)	30	30	30	30
Ratio $\frac{B_2H_6}{SiH_4}$	0.009	0.009	0.009	0.009
Ratio$\frac{CH_4}{CH_4+SiH_4}$	0.7	0.7	0.7	0.7
Power(W)	50	50	50	50

As it is shown in the Table 3.16, although SiH_4 flow rate is kept constant at 11 sccm the deposition rate decreases by increasing the H_2 flow rate. It is known that the H incorporation into the structure saturates the gap states and increases optical band gap. However, in this set the optical band gap of thin film decreases by increasing the H_2

flow rate. The reduction in the optical band gap is due to decrease in growth ratio rate so Si-Si bonds increases. This will lead to decrease of H content in the structure.

Table 3.17. *Characteristic parameters for p-a-SiC:H with CH_4 at 30 sccm for different hydrogen*

Characteristic	*p-a-SiC:H-10*	*p-a-SiC:H-11*	*p- a-SiC:H-12*	*p- a-SiC:H-13*
Thickness(nm)	63	60	57	51
Band gap(eV) Tauc plot	2.16	2.06	1.80	1.60
Band gap(eV) ellipsometry	2.10	2.05	1.88	1.70

It is mentioned in the studies related to the FTIR results at high rate H_2 dilution that the Si-H related vibrational bonds frequency may shift as the dilution increases. The wagging bond goes to lower wavenumbers and the stretching bond may shift to higher wavenumbers[32].

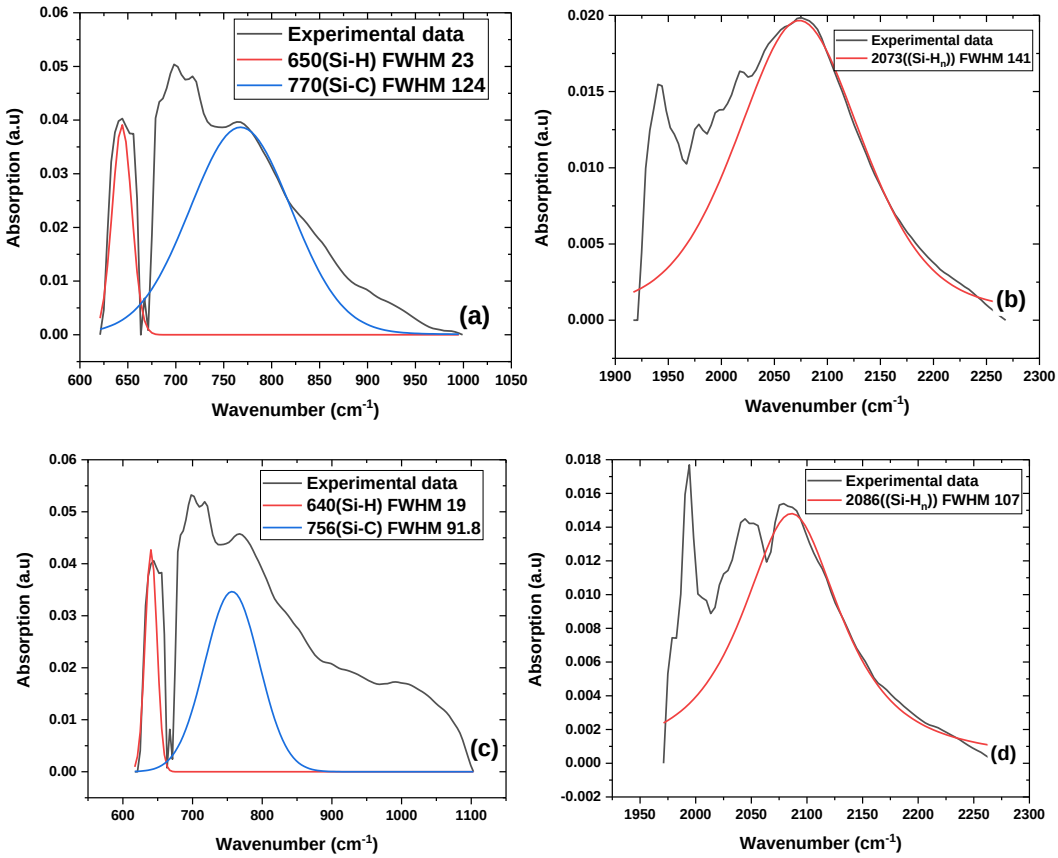

Figure 3.20. FTIR spectra for p-a-SiC:H-10(a and b) and p-a-SiC:H-11 (c and d) with CH_4 at 30 sccm for different hydrogen flow rates

The FTIR spectrum of this set is depicted in Figure 3.20 and Figure 3.21. As H_2 flow rate increases in this set from 200 sccm to 500 sccm, intensity of Si-H bonds (wagging and stretching) decreases which shows decrease of H incorporation in the a-Si structure also, it can be due to the decrease in the deposition rate. These results are in accordance with decrease in the optical band gap. Reduction in the Si-H bonds leads to a raise in the Si-Si bonding, which it may explain the upsurge in the intensity of Si-C bond at 770cm^{-1}. In addition, as the H_2 flow rate increases at 1000 cm^{-1} a band develops which can be related to the CH_n groups[16].

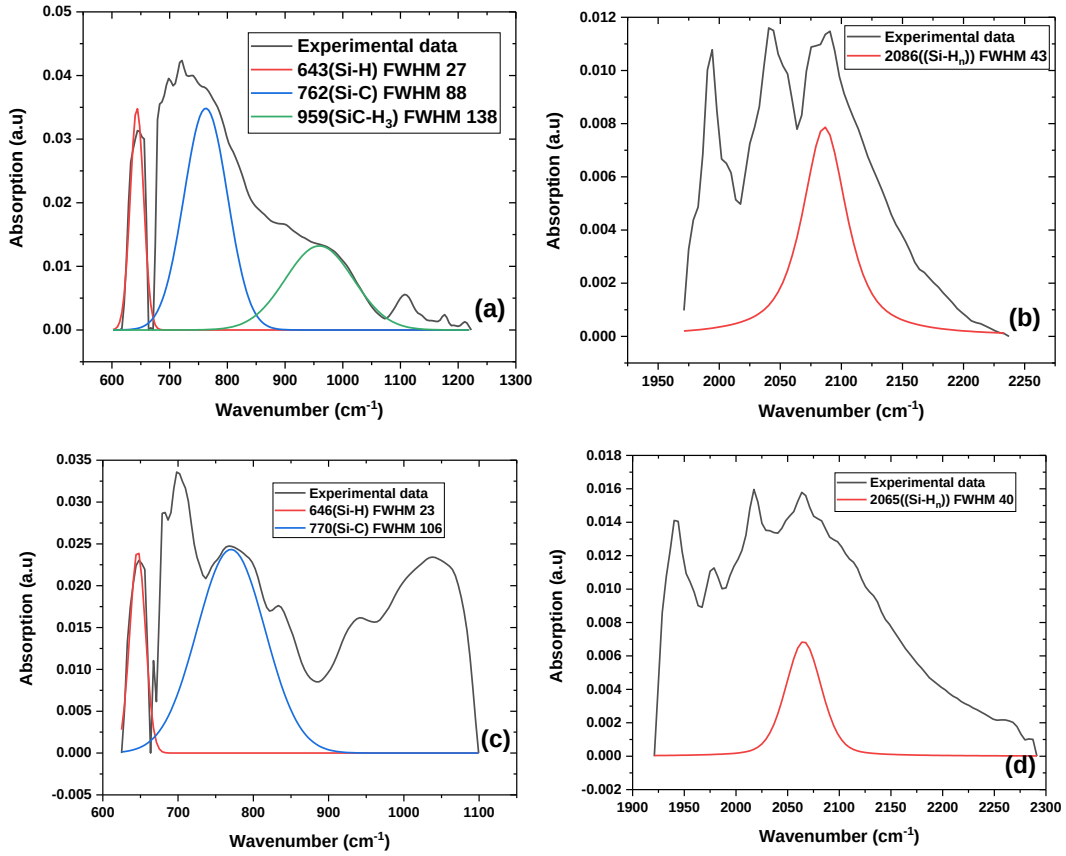

Figure 3.21. FTIR spectra for p-a-SiC:H-12(a and b) and p-a-SiC:H-13 (c and d) with CH_4 at 30 sccm for different hydrogen flow rates

Hydrogen content is calculated from the Si-H vibrational modes at 600-700 cm^{-1} (wagging) and 2000-2100 cm^{-1}(stretching) Tabled in Table 3.18. Which shows that the H content decreases as the H_2 flow rate increases from 200 sccm to 500 sccm.

Table 3.18. *Hydrogen content in p-a-SiC:H at 50W for different H_2 flow rates*

Characteristic	*p-a-SiC-10*	*p-a-SiC-11*	*p-a-SiC-12*	*p-a-SiC-13*
H_2 flow (sccm)	200	300	400	500
Hydrogen concentration (Si-H at 640 cm^{-1})	3.5%	3%	2%	1%
Hydrogen concentration (Si-H at 2090 cm^{-1})	1.6%	0.7%	0.1%	0.02%

XPS spectrum for p-a-SiC:H-10 sample in Figure3.22(a) demonstrates that the incorporated C in the film exist in Si-C, C-C/C-H, and C=C bonds with binding energy of 283.4 eV,284.5 eV, and 285.2 eV respectively. The binding energies are in accordance with the literature survey inserted in Table 3.15. B related peak in the XPS result reveals high B related bonds in the structure, as it is mentioned in chapter 2 the XPS detection limitation is in range of 0.1-1.0 % atomic percentage (0.1%=1 part per thousand=1000ppm) so the B is hard to be detected in the a-Si and c-Si structure. Binding energy of B-B/B-Si bond is inserted in Table 3.14. The B 1s detected in sample p-a-SiC:H-10 is shown in Figure 3.22. Binding energy of B bonds (B-B/B-Si) in this sample is around 187 eV.

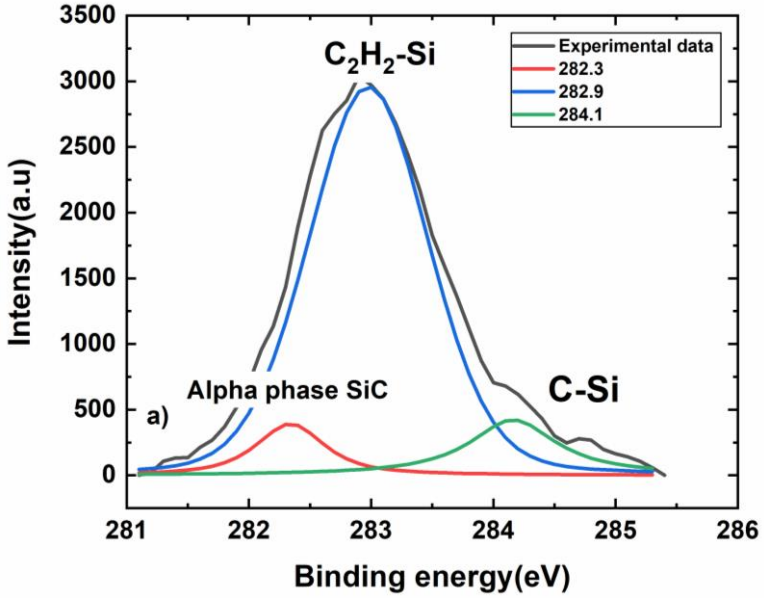

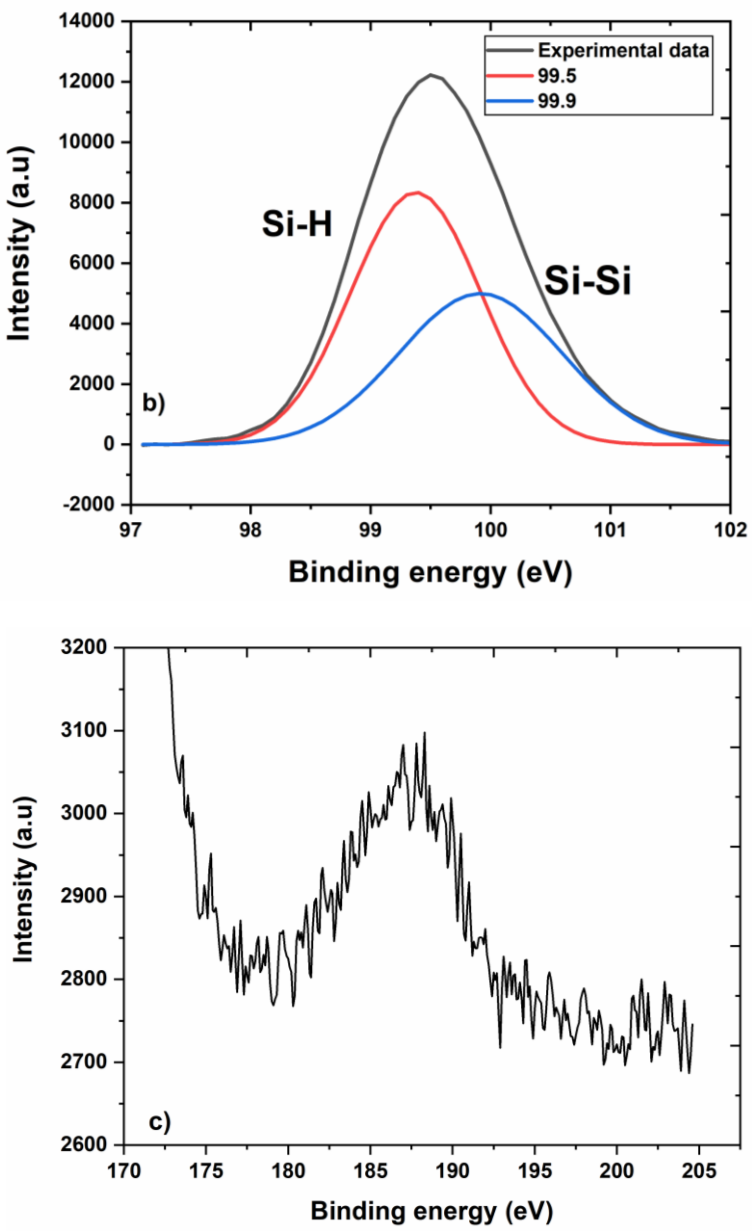

Figure 3.22. XPS spectra for p-a-SiC:H-10 a) Si 2p b) C 1s B 1s

Table 3.19. *Atomic concentrations of C1s, Si2p, and B1s for p-a-SiC:H-10 sample*

p-a-SiC:H-10	*C1s*	*Si2p*	*B1s*
No ion etching	33.38	52.36	14.24
After ion etching for 3 min	16.21	68.06	15.72

Atomic concentrations of existed elements in sample p-a-SiC:H-10 is inserted in Table 3.19. the atomic concentration for B1s is really high if one may consider the detection limit of XPS. However, the conductivity of the film is really low which is expected to happen as it is mentioned in chapter 1.

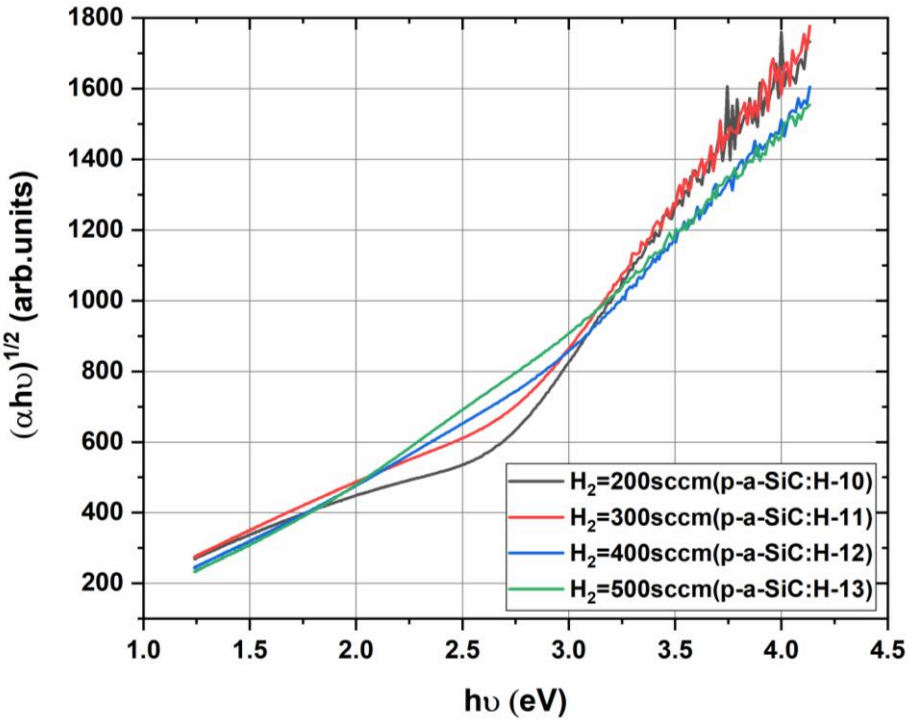

Figure 3.23. Tauc plot for p-a-SiC with CH_4 at 30 sccm for different hydrogen content

It can be seen that the tauc plot of the samples become more straight as the H_2 flow rate increases, and the thickness and optical band gap decreases as it is shown in Figure 3.23.

From results of the last experiment, H_2 flow rate of 200 sccm is chosen as the best growth parameters. As a reference sample of p-a-SiC:H deposited at 200 sccm H_2 flow rate by means of no CH_4 flow during growth, two p type a-Si:H samples are deposited as it is mentioned in the Table 3.20. During deposition of p-a-Si:H at 70W, the substrate temperature is increased to 275°C unintentionally as explained before.

Table 3.20. *Deposition parameters for p-a-Si:H for different powers*

Deposition parameters	*p-a-Si:H-58*	*p-a-Si:H-59*
Temperature(°C)	200	200
Pressure (Torr)	1	1
Deposition Duration (min)	7	4
SiH_4 flow rate (sccm)	11	11
B_2H_6 flow rate (sccm)	5	5
H_2 flow rate (sccm)	200	200
CH_4 flow rate (sccm)	0	0
Ratio $\frac{B_2H_6}{SiH_4}$	0.009	0.009
Ratio$\frac{CH_4}{CH_4+SiH_4}$	0	0
Power(W)	50	70

Optical band gap values of reference samples are found as 1.65eV both from the tauc plot and ellipsometry measurements as shown in Table 3.21 which are expected values for p-a-Si:H layers. Dark conductivity measurements are showed that p-a-Si:H-58 has very low conductivity whereas p-a-Si:H-59 has a conductivity around 4.5×10^{-5} σ/cm which is low for a p-a-Si:H in compare to the literature.

Table 3.21. *Characterization parameters for p-a-Si:H for different powers*

Characteristic	*p-type a-Si-58*	*p-type a-Si-59*
Thickness(nm)	98	68
Band gap(eV)Tauc plot	165	1.64
Band gap(eV) ellipsometry	1.65	1.64

For a-SiC:H samples with high H_2 flow rate, at 50 W power three CH_4 flow rates are chosen as 10,15,20 sccm. Doping flow rate is kept low at 0.009 to see effect of High H_2 flow rate.

Table 3.22. *Deposition parameters for p-a-SiC:H at 50 W power*

Deposition parameters	*p-a-SiC:H-14*	*p-a-SiC:H-15*	*p-a-SiC:H-16*
Temperature(°C)	200-200	200-200	200-200
Pressure (Torr)	1	1	1
Deposition Duration (min)	7	7	7
SiH_4 flow rate (sccm)	11	11	11
B_2H_6 flow rate (sccm)	5	5	5
H_2 flow rate (sccm)	200	200	200
CH_4 flow rate (sccm)	10	15	20
Ratio $\frac{B_2H_6}{SiH_4}$	0.009	0.009	0.009
Ratio$\frac{CH_4}{CH_4+SiH_4}$	0.47	0.57	0.64
Power(W)	50	50	50

Deposition rate is relatively low compared to previous sets since the H_2 flow rate is high enough, the incorporation of H into the structure is high so the optical band gap increases as it is indicated in Table 3.23. By increasing the CH_4 flow rate the optical band gaps calculated from the tauc plots of Figure 3.24 remain in the same range. However, calculated optical band gaps from the ellipsometry increase slightly.

Table 3.23. *Characterization parameters for p-a-SiC:H samples at 50 W power*

Characteristic	*p-a-SiC:H-14*	*p-a-SiC:H-15*	*p-a-SiC:H-16*
Thickness(nm)	46	37	35
Band gap(eV) Tauc plot	1.90	1.80	1.90
Band gap(eV) ellipsometry	1.90	2.10	2.20

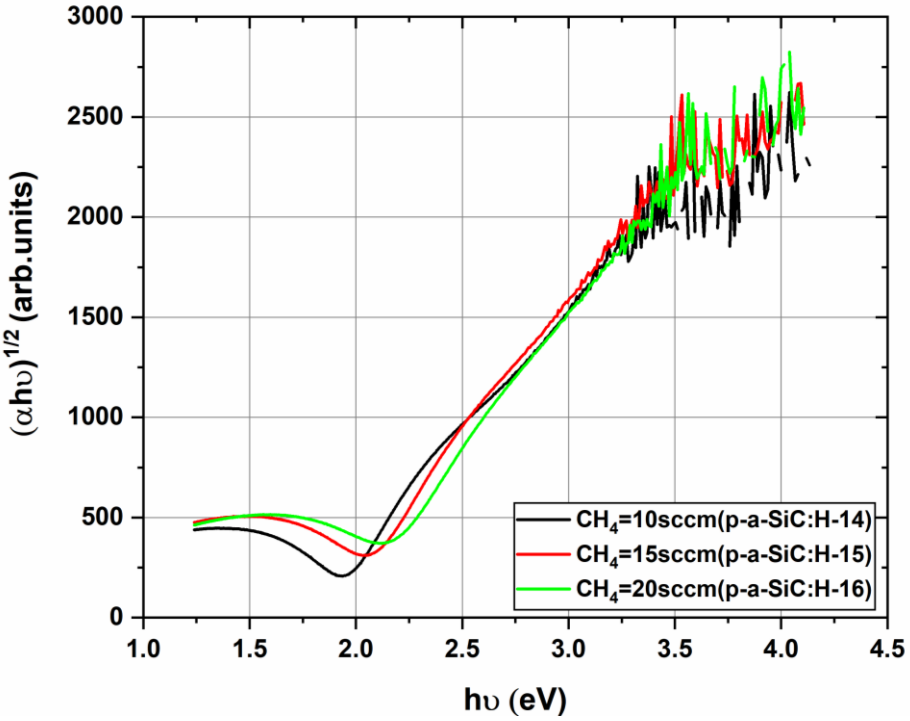

Figure 3.24. Tauc plot for p-a-SiC:H with different CH_4 flow rates at 50 W

FTIR spectrum for the samples p-a-SiC:H14-15-16 are depicted in Figure3.25(a-b), (c-d), (e-f) respectively. In the Figure3.25(a) the Si-C bond related peak at 778 cm^{-1} has higher intensity than other samples in this set, which shows that 50W for CH_4 flow rate at 10 sccm, provides more energy to break the CH_4 bonds in order to re-bond with Si and incorporate in the a-Si structure. By increasing CH_4 flow rate this energy will not be enough. Intensity of Si-H stretching bond also decreases as the CH_4 flow rate increases, which decreases the total H content inside the thin film as well.

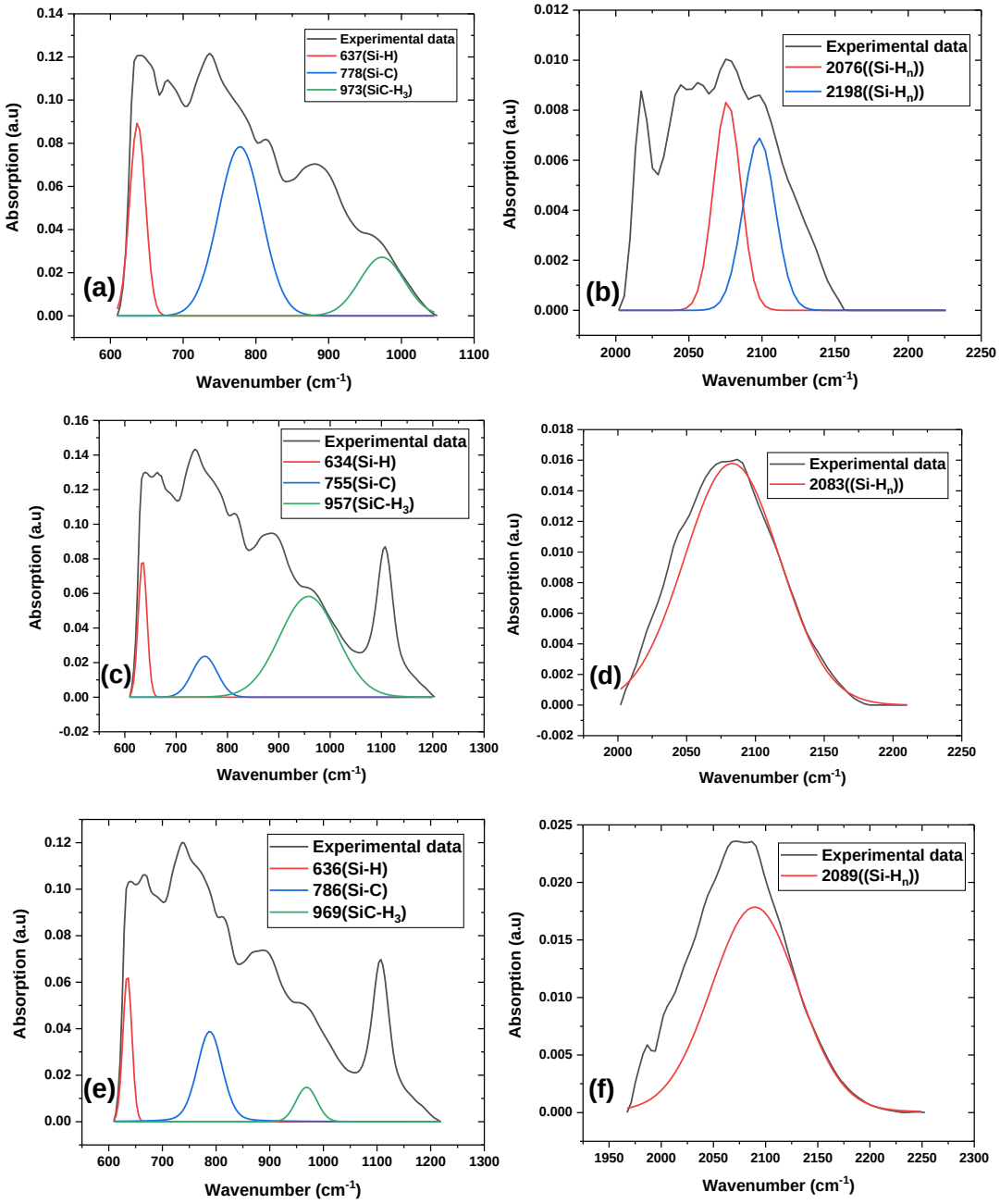

Figure 3.25. FTIR spectra for p-a-SiC:H-14(a-b), p-a-SiC:H-15(c-d), p-a-SiC:H-16(e-f)samples

The samples deposited at 50 W have very low conductivity properties compared to previous ones. On one hand by increasing power, we aim to achieve relatively high conductivity values. On the other hand, it is expected that by increasing power to 70W, sufficient energy will be provided to the CH_4 gas to decompose, resulting high optical

band gap values. For this reason, the designed deposition parameters at 70W power is given in Table 3.24.

Table 3.24. *Deposition parameters for p-a-SiC:H at 70 W power*

Deposition parameters	*p-a-SiC:H-17*	*p-a-SiC:H -18*	*p-a-SiC:H -19*
Temperature(°C)	200	200	200
Pressure (Torr)	1	1	1
Deposition Duration (min)	4	4	4
SiH_4 flow rate (sccm)	11	11	11
B_2H_6 flow rate (sccm)	5	5	5
H_2 flow rate (sccm)	200	200	200
CH_4 flow rate (sccm)	10	15	20
Ratio $\frac{B_2H_6}{SiH_4}$	0.009	0.009	0.009
Ratio$\frac{CH_4}{CH_4+SiH_4}$	0.47	0.57	0.64
Power(W)	70	70	70

Tauc plot and ellipsometry results are given in Table 3.25 and Figure 3.26. Deposition rate of thin film with higher power is higher in comparing to 50W as expected. Increasing power leads to an increase in the optical band gap as well which shows higher C incorporation to film is achieved by higher CH_4 flow rate.

Table 3.25. *Characterization parameters for p-a-Si:H at 70 W power*

Characteristic	*p-a-SiC:H-17*	*p-a-SiC:H -18*	*p-a-SiC:H -19*
Thickness(nm)	30	27	27
Band gap(eV) Tauc plot	2.00	2.00	2.13
Band gap(eV) ellipsometry	2.23	2.30	2.30

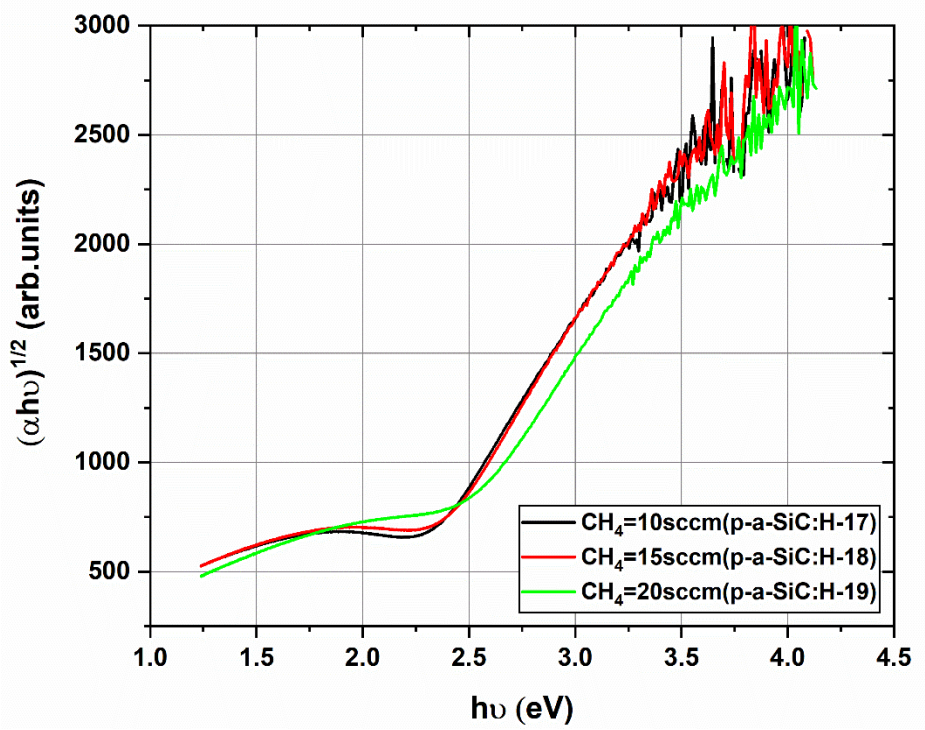

Figure 3.26. Tauc plot for p-a-SiC at 70 W power

Figure 3.27 shows the FTIR spectrum for samples p-a-Si-C:H-17-18-19. As the CH_4 flow rate increases the Si-C bond intensity increases which show the more C incorporation in the structure. However, the SiC-H_3 peak intensity is high in the all three samples.

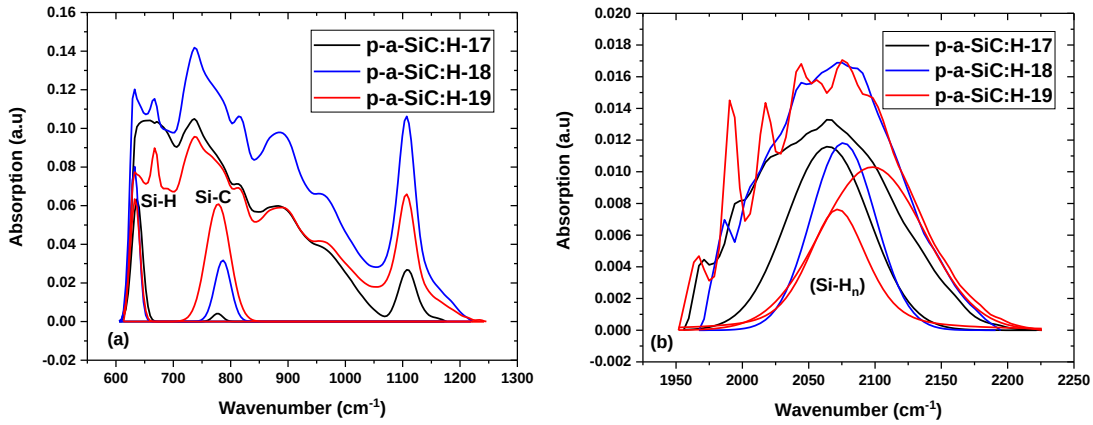

Figure 3.27. FTIR spectra for p-a-SiC:H samples with 70 W power

Raman measurement has been done in order to investigate the Si-Si and C-C bonds since they are not infrared active bonds. Also, existing nanocrystals inside the samples with low H content is investigated as well[63]. Raman measurements done at room temperature. As it can be seen in the Figure 3.28 and Figure 3.29, there are two bands between the 0-500 cm^{-1} and 500-1000cm^{-1}. According to the literature the observed band in the 0-500 cm^{-1} region corresponds to the a-Si and the band in the 500-1000cm^{-1} corresponds to the infrared absorption of Si-C bond[63].

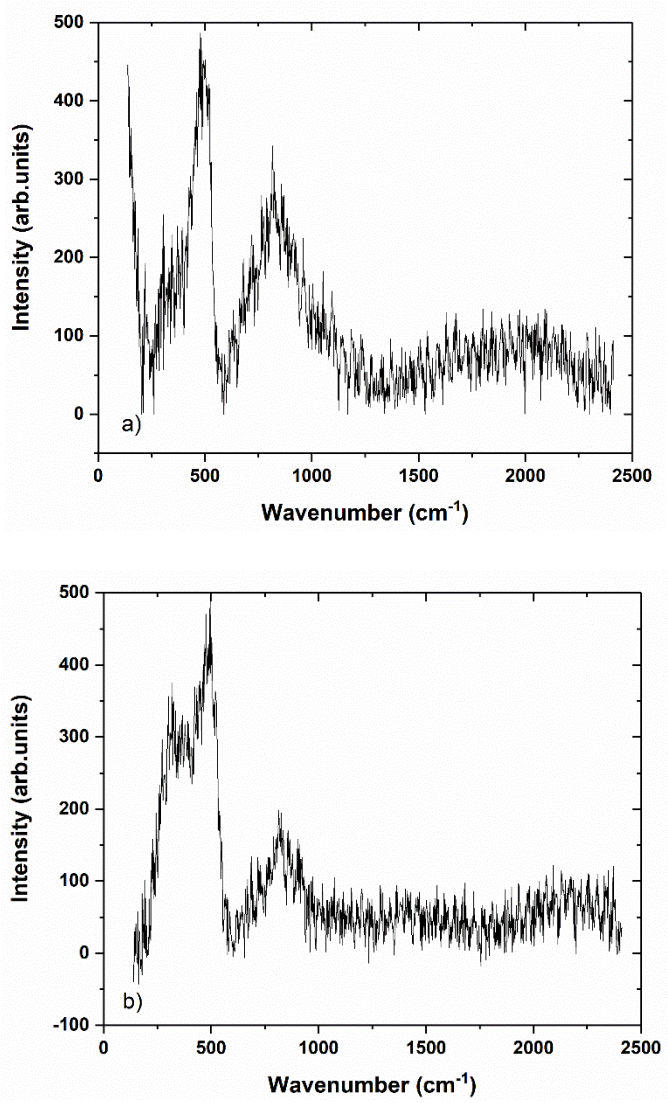

Figure 3.28. Raman spectra for p-a-SiC:H-10 (a) and p-a-SiC:H-11 (b)

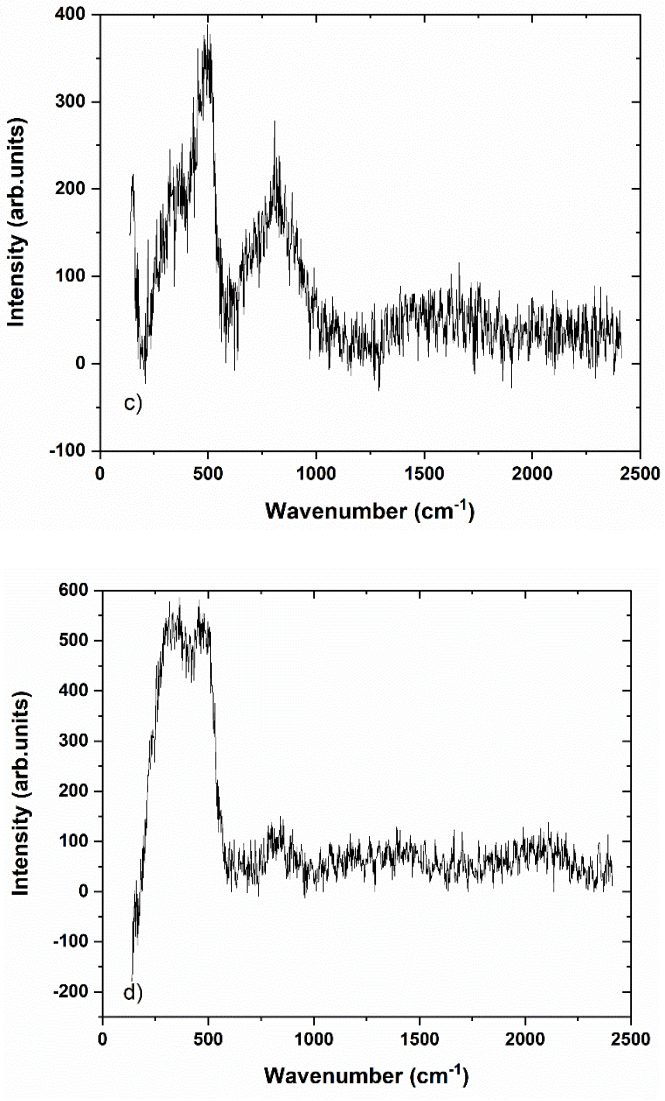

Figure 3.29. Raman spectra for p-a-SiC:H-12 (c) and p-a-SiC:H-13(d)

3.4. Effect of Silane and Diborane Flow Rate Variation

By comparing the characteristics of the samples, the best deposition parameters are selected from previous sets so far. RF power of 50 W gives sufficient energy to break the molecules and plasma, and H_2 flow rate is selected as 120 sccm since the higher flow rates lead to a higher optical band gap which decreased the conductivity drastically. In this set by altering the SiH_4 and B_2H_6 flow rates, the conductivity and optical behavior is investigated. In addition, to compare the p-a-SiC:H results with reference p-a-Si:H samples are deposited as given in Table 3.26.

Table 3.26. *Deposition parameters for p-a-Si:H for different SiH_4 and B_2H_6 flow rates*

Deposition parameters	*p-a-Si:H-60*	*p-a-Si:H-61*	*p-a-Si:H-62*	*p-a-Si:H-63*
Temperature(°C)	200	200	200	200
Pressure (Torr)	1	1	1	1
Deposition Duration (min)	7	7	7	7
SiH_4 flow rate (sccm)	20	20	15	15
B_2H_6 flow rate (sccm)	35	40	35	40
H_2 flow rate (sccm)	120	120	120	120
CH_4 flow rate (sccm)	0	0	0	0
Ratio $\frac{B_2H_6}{SiH_4}$	0.035	0.04	0.046	0.053
Ratio$\frac{CH_4}{CH_4+SiH_4}$	0	0	0	0
Power(W)	50	50	50	50

The optical band gap values and thicknesses of this set are mentioned in the Table 3.27. B doped a-Si has direct optical band gap and it is in range of 1.6 eV~1.65 eV[64].

Table 3.27. *Characterization parameters for p-a-Si:H for different SiH_4 and B_2H_6 flow rates*

Characterization	*p-a-Si:H-60*	*p-a-Si:H-61*	*p-a-Si:H-62*	*p-a-Si:H-63*
Doping Ratio	0.035	0.04	0.046	0.053
Thickness(nm)	167	152	126	135
Band gap(eV)Tauc plot	1.67	1.79	1.72	1.74
Band gap(eV) ellipsometry	1.62	1.63	1.63	1.63

Band gap (from ellipsometry) doesn't change so much with SiH_4 and B_2H_6 variation however, optical band gap calculated from the tauc plot increases as doping ratio increases. The tauc plot is shown in the Figure 3.30 and the zoomed linear part is shown in the Figure 3.29.

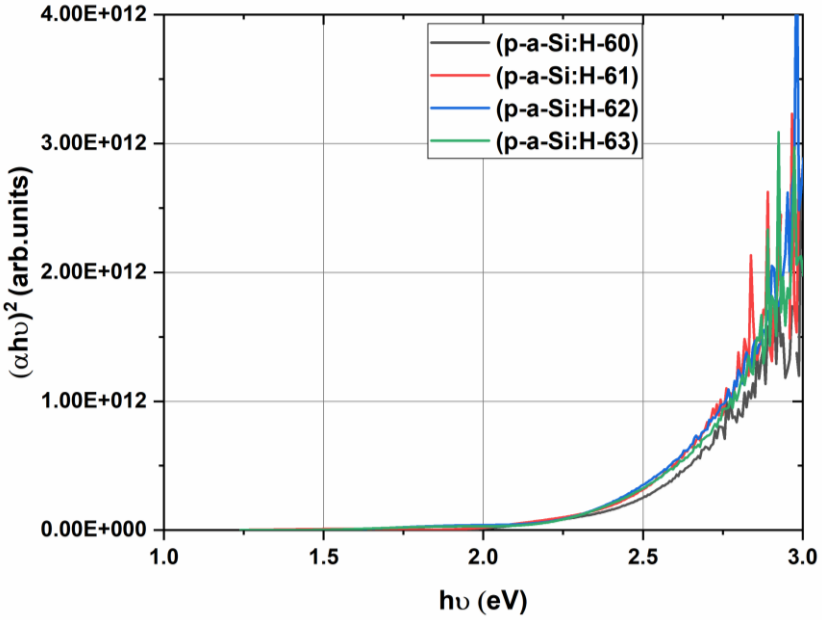

Figure 3.30. Tauc plot for p-a-Si:H samples with different SiH_4 and B_2H_6 flow rates

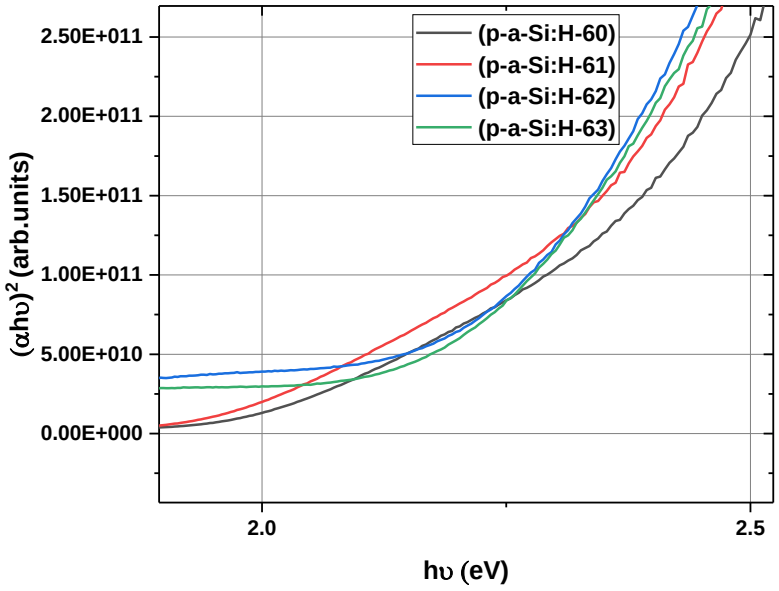

Figure 3.31. Linear part of the tauc plot spectras p-a-Si:H samples with different SiH_4 and B_2H_6 flow rates

The conductivity of samples is shown in Figure 3.31, as the B_2H_6 flow rate increases for p-a-Si:H 61, the conductivity of samples p-a-Si:H 61 decreases in compare to p-aSi:H-60. This may be due to the higher B in the structure and optical band gap

calculated from the tauc plot is increased as well. However, the conductivity is photosensitive for both samples. For samples p-a-Si:H-62 and p-a-Si:H-63 the SiH_4 flow rate decreased to 15 sccm but, the B_2H_6 flow rate increases from 35 sccm to 40 sccm. The deposition rate for the two samples decreases since the SiH_4 flow rate decreases.

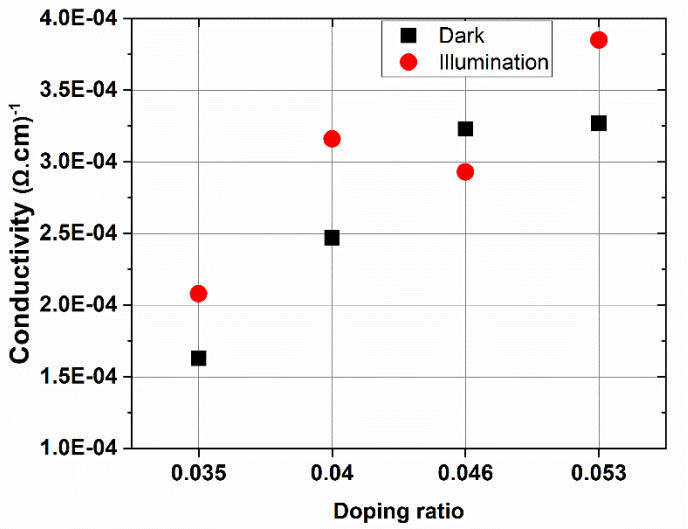

Figure 3.32. Conductivity for p-a-Si:H samples with different SiH_4 and B_2H_6 flow rates

After reference p-type a-Si:H depositions, the CH_4 flow rate is introduced during growth to compare and identify relation between reference and p-type a-SiC:H layers. Table 3.28 shows deposition parameters of p-type a-SiC:H layers.

Table 3.28. *Deposition parameters for p-a-SiC:H with CH_4 at 30 sccm and different doping ratio*

Deposition parameters	*p-a-SiC:H-20*	*p-a-SiC:H-21*	*p-a-SiC:H-22*	*p-a-SiC:H-23*
Temperature(°C)	200	200	200	200
Pressure (Torr)	1	1	1	1
Deposition Duration (min)	7	7	7	7
SiH_4 flow rate (sccm)	20	20	15	15
B_2H_6 flow rate (sccm)	35	40	35	40
H_2 flow rate (sccm)	120	120	120	120

CH_4 flow rate (sccm)	30	30	30	30
Ratio $\frac{B_2H_6}{SiH_4}$	0.035	0.04	0.046	0.053
Ratio$\frac{CH_4}{CH_4+SiH_4}$	0.6	0.6	0.6	0.6
Power(W)	50	50	50	50

Both ellipsometry and Tauc plot results are shown in Table 3.32. From Tauc plot, band gap results are comparable with each other around 1.9eV. However, the ellipsometry results show that increasing doping ratio leads decrease in optical band gap except p type a-SiC:H 22.

Table 3.29. *Characterization parameters for p-a-SiC:H with CH_4 at 30 sccm and doping ratio*

Characterization	*p-a-SiC:H-20*	*p-a-SiC:H-21*	*p-a-SiC:H-22*	*p-a-SiC:H-23*
Doping Ratio	0.035	0.04	0.046	0.053
Thickness(nm)	222	247	154	166
Band gap(eV) Tauc plot	1.90	1.82	1.80	1.92
Band gap(eV) ellipsometry	2.30	1.90	2.00	1.80

Conductivity of sample p-a-SiC:H-21 decreases in compare to p-a-SiC:H-20 as the B_2H_6 flow rate increases. For both p-a-SiC:H-22 and p-a-SiC:H-23 samples SiH_4 flow rate decreases and film become so resistive that for conductivity measurement, sensitive probes are used.

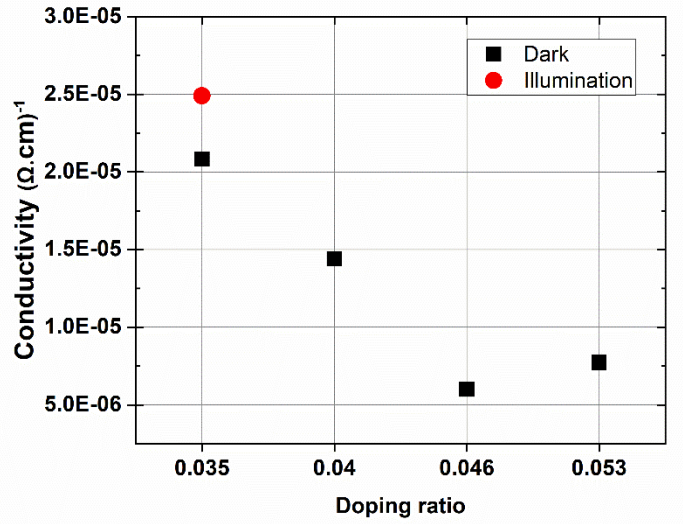

Figure 3.33. Conductivity for p-a-SiC:H samples with different SiH_4 and B_2H_6 flow rates

As it is also observed in analyzing the FTIR spectrum of the p-a-SiC:H in the Figure3.34(a) that the intensity of the Si-C related peak decreases as the doping ratio increases except for the p-a-SiC:H-22 as it is mentioned before. However, it is worth to mention that the intensity of the Si-C and Si-H (wagging) peaks that are observed have higher intensity in compare to the p-a-SiC:H samples deposited with H_2 flow rate of 200 sccm.

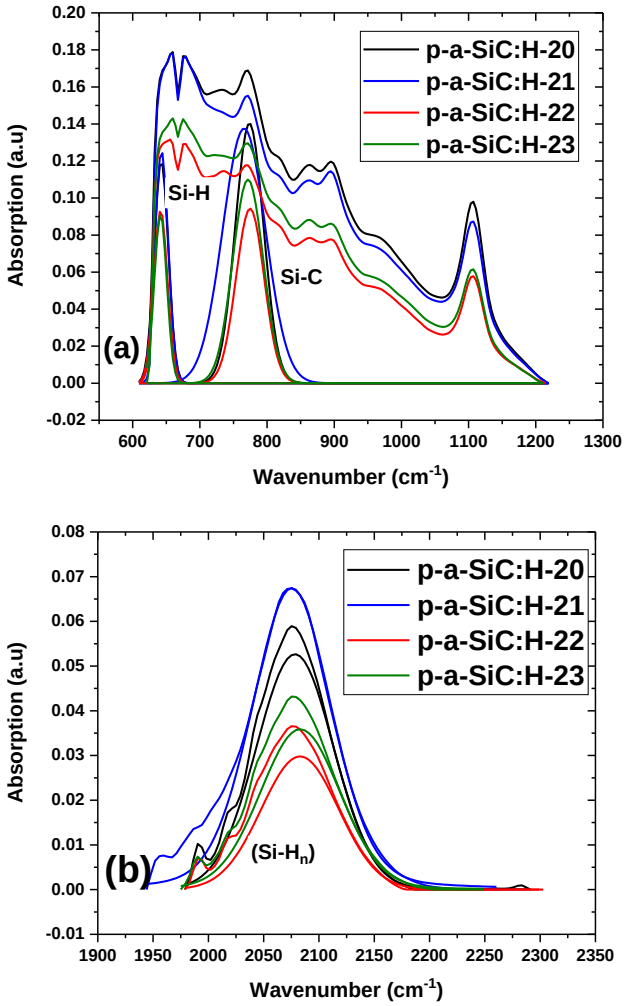

Figure 3.34. FTIR spectrum for p-a-SiC:H samples with different doping ratio

CHAPTER 4

CONCLUSION

C incorporation in the B doped a-Si:H network increases the disorder in the amorphous network which changes the optical and electrical properties of p-a-SiC. C bindings in the structure are dependent on the deposition condition. B doped a-SiC:H is generally deposited by the PECVD. In this study, we have investigated the effects of RF-power, CH_4, SiH_4, B_2H_6, and H_2 flow rates on the optical and electrical properties of p-a-SiC:H deposited by PECVD. First, we investigated RF-power and CH_4 flow rate variations. Based on the previous works we chose the precursor gases flow rates as H_2=120 sccm, B_2H_6=20 sccm, SiH_4=30 sccm. CH_4 flow rates varied from 10 to 30 sccm, and RF-power varied from 30 to 70W.

In order to observe the effect of power clearly, we kept precursor gas flow rates constant. For CH_4=10 sccm we have observed that as the power increases, optical band gap and conductivity increase as well, which shows that by increasing power, enough energy for decomposition of the CH_4 and dopant molecules are provided. In this set for sample with 50 W, XPS results showed that the C bonds in the sample do does not belong to the specific binding configuration. For the next set CH_4 kept at 20 sccm, it was observed that the optical band gap increases as the power increase. Conductivity improves as the power increases, however the most C concentration in the thin films, belongs to the sample with the lowest power. For the third set with CH_4=30 sccm, the power increased from 30 to 70 W. Same trend for optical band gap has been observed as for the previous sets. However, in this set for RF-power of 50 W, the largest incorporation of the C and B atom among these sets has been seen.

Next, based on the best parameters in terms of optical band gap and conductivity of the thin film,which we have achieved before, we investigated the H_2 flow rate

variation on the a-SiC formation. For precursor gasses, constant flow rates of CH_4=30 sccm, B_2H_6=5 sccm, SiH_4=11 sccm and RF-power=50 W are chosen. By increasing the H_2 from 200 sccm to 500 sccm we have observed that the deposition ratio, optical band gap decreases. From the FTIR results, we have seen that the reduction of H incorporation into the structure is the main reason for decreasing the optical band gap.

Finally, in order to investigate the effect of SiH_4 and B_2H_6 flow rates on the improvements of the p-a-SiC:H conductivity, as the doping ratio increase the conductivity decrease, because of the lower Si-C bonds within the structure.

In this work B doped a-SiC:H thin film has been investigated in order to achieve a window layer with high optical band gap and good conductivity in order to integrate on the SHJ and increase the absorption of the incident light and decrease the parasitic absorption. For future works, it should be investigated the effect of the integrated p type a-SiC layer on SHJ solar cells performance and the contact resistivity between p type a-SiC and TCO layer.

REFERENCES

[1] R. Williams, “Becquerel photovoltaic effect in binary compounds,” *J. Chem. Phys.*, vol. 32, no. 5, pp. 1505–1514, 1960.

[2] “Https://www.nobelprize.org/prizes/physics/1921/summary/.” .

[3] R. S. Ohl, “Light-sensitive electric device,” *United States Pat. Off. 2402662*, pp. 1–14, 1941.

[4] “Https://www.aps.org/publications/apsnews/200904/physicshistory.cfm.” [Online]. Available: https://www.aps.org/publications/apsnews/200904/physicshistory.cfm. [Accessed: 05-Sep-2019].

[5] A. Descoeudres *et al.*, “Silicon Heterojunction Solar Cells: Towards Low-cost High-Efficiency Industrial Devices and Application to Low-concentration PV,” *Energy Procedia*, vol. 77, pp. 508–514, 2015.

[6] M. M. Lunardi, J. P. Alvarez-Gaitan, N. L. Chang, and R. Corkish, “Life cycle assessment on PERC solar modules,” *Sol. Energy Mater. Sol. Cells*, vol. 187, pp. 154–159, 2018.

[7] S. V. Obydenkova and J. M. Pearce, “Technical viability of mobile solar photovoltaic systems for indigenous nomadic communities in northern latitudes,” *Renew. Energy*, vol. 89, pp. 253–267, 2016.

[8] “http://www.tindosolar.com.au/learn-more/poly-vs-mono-crystalline/.” [Online]. Available: http://www.tindosolar.com.au/learn-more/poly-vs-mono-crystalline/. [Accessed: 05-Sep-2019].

[9] “http://www.solarshine.net/solarcellhistory.php.” [Online]. Available: http://www.solarshine.net/solarcellhistory.php. [Accessed: 05-Sep-2019].

[10] “Https://energyinformative.org/best-thin-film-solar-panels-amorphous-cadmium-telluride-cigs/.” .

[11] “Http://www.greentechmedia.com/articles/read/Honoring-the-fallen-solarsoldiers.” .

[12] F. Es, “Fabrication and Characterization of single crystal silicon solar cells,” 2010.

[13] W. G. J. H. . Van sark, F. Roca, and L. Korte, *Physics and technology of amorphous-crystalline heteronstrutures sillicon solar cells.* 2012.

[14] "Https://www.pveducation.org/pvcdrom/manufacturing-si-cells/solid-state-diffusion." [Online]. Available: https://www.pveducation.org/pvcdrom/manufacturing-si-cells/solid-state-diffusion. [Accessed: 05-Sep-2019].

[15] G. Nogay, "Full-area passivating contacts with high and low thermal budgets: Solution for high-efficiency c-Si solar cells," 2018.

[16] J. J. Gandía, M. T. Gutiérrez, and J. Cárabe, "Properties of p-type amorphous silicon carbide window layers prepared using boron trifluoride," *Sol. Energy Mater. Sol. Cells*, vol. 29, no. 2, pp. 139–148, 1993.

[17] B. W. H. Van De Loo, *Atomic-layer-deposited surface passivation schemes for silicon solar cells*. 2017.

[18] R. Madaka, V. Kanneboina, and P. Agarwal, "Enhanced performance of amorphous silicon solar cells (110 °c) on flexible substrates with a-SiC:H(p) window layer and H2 plasma treatment at n/i and i/p interface," *Semicond. Sci. Technol.*, vol. 33, no. 8, 2018.

[19] C.-C. Yang, "Hydrogenated Amorphous Silicon Carbide Prepared using DC Saddle Field PECVD for Photovoltaic Applications," p. 129, 2011.

[20] A. Shah, *Thin film silicon solar cells*. 2010.

[21] A. H. M. Smets, W. M. M. Kessels, and M. C. M. Van de Sanden, "Vacancies and voids in hydrogenated amorphous silicon," *Appl. Phys. Lett.*, vol. 82, no. 10, pp. 1547–1549, 2003.

[22] F. Alvarez, M. Sebastiani, F. Pozzilli, P. Fiorini, and F. Evangelisti, "Influence of hydrogen dilution on the optoelectronic properties of glow discharge amorphous silicon carbon alloys," *J. Appl. Phys.*, vol. 71, no. 1, pp. 267–272, 1992.

[23] W. Beyer, "Microstructure characterization of plasma-grown a-Si:H and related materials by effusion of implanted helium," *J. Non. Cryst. Solids*, vol. 338–340, no. 1 SPEC. ISS., pp. 232–235, 2004.

[24] D. Suwito, "Intrinsic and doped amorphous silicon carbide films for the surface passivation of silicon solar cells," *PhD thesis*, 2011.

[25] D. E. Polk, “Structural model for amorphous silicon and germanium,” *J. Non. Cryst. Solids*, vol. 5, no. 5, pp. 365–376, 1971.

[26] P. C. Kelires, “Structure and chemical ordering in amorphous silicon carbide alloys.,” *Epl*, vol. 14, no. 1, pp. 43–48, 1991.

[27] L. Wang, “Deposition and Characterisation of Amorphous and Nanocrystalline SiC,” no. September, 2009.

[28] H. Shaik, K. H. Thulasi Raman, and G. M. Rao, “Influence of Si-C bond density on the properties of a-Si 1-x C x thin films,” *Appl. Surf. Sci.*, vol. 258, no. 7, pp. 2989–2996, 2012.

[29] P. L. S. V.I IvAshchenko, L.A Ivashchenko, “V.I IvAshchenko, L.A Ivashchenko, P.L. Srynsckyy," AB initio simulations of liquid and amorphous SiC and SiCN ",” *Inst. Probl. Mater. Sci.*, vol. 50, no. 6, p. 1143, 2008.

[30] T. Maruyama and S. Mitani, “The network structure of amorphous silicon-carbon alloy,” *J. Non. Cryst. Solids*, vol. 319, no. 3, pp. 219–224, 2003.

[31] A. Shah, *Thin film silicon solar cells*. .

[32] U. Kroll, J. Meier, A. Shah, S. Mikhailov, and J. Weber, “Hydrogen in amorphous and microcrystalline silicon films prepared by hydrogen dilution,” *J. Appl. Phys.*, vol. 80, no. 9, pp. 4971–4975, 1996.

[33] I. Pereyra, C. A. Villacorta, M. N. P. Carreño, R. J. Prado, and M. C. A. Fantini, “Highly ordered amorphous silicon-carbon alloys obtained by RF PECVD,” *Brazilian J. Phys.*, vol. 30, no. 3, pp. 533–540, 2005.

[34] A.A. Langford, “Infrared absorption,” *J. Chem. Inf. Model.*, vol. 53, no. 9, pp. 1689–1699, 2013.

[35] O. C. N. Ross, K. Shrestha, “Characterization of Boron Doped Amorphous Silicon Films by Multiple Internal Reflection Infrared Spectroscopy,” *J. Chem. Inf. Model.*, vol. 53, no. 9, pp. 1689–1699, 2013.

[36] B. G. Streetman, • Sanjay, and K. Banerjee, *Global edition Solid State electronic devices Seventh edition*. .

[37] W. E. Spear and P. G. Le Comber, “Substitutional doping of amorphous silicon,” *Solid State Commun.*, vol. 88, no. 11–12, pp. 1015–1018, 1993.

[38] J. B. Boyce and S. E. Ready, “Nuclear magnetic resonance investigation of H,

H2 and dopants in hydrogenated amorphous silicon and related materials," *Phys. B Phys. Condens. Matter*, vol. 170, no. 1–4, pp. 305–319, 1991.

[39] J. Huran, "Electrical and Structural Properties of Amorphous Silicon Carbide and Its Application for Photovoltaic Heterostructures," vol. 4, no. 3, pp. 17–19, 2011.

[40] T. Inoue, T. Tanaka, M. Konagai, and K. Takahashi, "Electronic and optical properties of p-type amorphous silicon and wide band-gap amorphous silicon carbide films prepared by photochemical vapor deposition," *Appl. Phys. Lett.*, vol. 44, no. 9, pp. 871–873, 1984.

[41] F. Alvarez, H. L. Fragnito, and I. Chambouleyron, "Electroluminescence from amorphous silicon carbide heterojunctions under reverse biased conditions," *J. Appl. Phys.*, vol. 63, no. 1, pp. 244–246, 1988.

[42] Y. Y. Wang, K. Kusumoto, and C. J. Li, "XPS Analysis of SiC Films Prepared by Radio Frequency Plasma Sputtering," *Phys. Procedia*, vol. 32, pp. 95–102, 2012.

[43] S. Y. Myong, S. S. Kim, and K. S. Lim, "Improvement of pin-type amorphous silicon solar cell performance by employing double silicon-carbide p-layer structure," *J. Appl. Phys.*, vol. 95, no. 3, pp. 1525–1530, 2004.

[44] E.Dönerçark, "'Surface preperation, passivation and patterning techniquesused in siicon based heterojunstion solar cells,'" 2017.

[45] E. Ozkol, "Opitimization of PECVD," 2015.

[46] S. Janz, "Amorphous Silicon Carbide for Photovoltaic Applications," 2006.

[47] W. T. Tsang, E. F. Schubert, and J. E. Cunningham, "Doping in semiconductors with variable activation energy," *Appl. Phys. Lett.*, vol. 60, no. 1, pp. 115–117, 1992.

[48] G. Nogay, "Full-area passivating contacts with high and low thermal budgets: Solution for high-efficiency c-Si solar cells," EPFL, 2018.

[49] "https://xpssimplified.com/elements/carbon.php." [Online]. Available: https://xpssimplified.com/elements/carbon.php. [Accessed: 05-Sep-2019].

[50] L.C. Feldman and J.W. Mayer, "Fundamentals of surface and thin film analysis," *Nucl. Instruments Methods Phys. Res. Sect. B*, vol. 26, p. 1987, 1987.

[51] S. De Wolf and M. Kondo, “Abruptness of a-Si:Hc-Si interface revealed by carrier lifetime measurements,” *Appl. Phys. Lett.*, vol. 90, no. 4, pp. 1–4, 2007.

[52] S. Janz, “Amorphous silicon carbide for photovoltaic applications,” 2006.

[53] B. P. Swain, “The analysis of carbon bonding environment in HWCVD deposited a-SiC:H films by XPS and Raman spectroscopy,” *Surf. Coatings Technol.*, vol. 201, no. 3–4, pp. 1589–1593, 2006.

[54] D. H. Zhang and D. Haneman, “Band gap and activation energy in amorphous silicon doping-modulated superlattices,” *Appl. Phys. Lett.*, vol. 52, no. 17, pp. 1392–1394, 1988.

[55] F. J. De Hidalga-w and A. P, “Properties of Boron Doped Amorphous Silicon Films Obtained with a Low Frequency Plasma,” *Phys. Rev.*, vol. 19, no. 4, pp. 2055–2055, 1979.

[56] S. Kennou, “An x-ray photoelectron spectroscopy and work-function study of the Er/α-SiC(0001)interface,” *J. Appl. Phys.*, vol. 78, no. 1, pp. 587–589, 1995.

[57] J. R. Waldrop and R. W. Grant, “Formation and Schottky barrier height of metal contacts to β-SiC,” *Appl. Phys. Lett.*, vol. 56, no. 6, pp. 557–559, 1990.

[58] H. Sezen and S. Suzer, “Communication: Enhancement of dopant dependent x-ray photoelectron spectroscopy peak shifts of Si by surface photovoltage,” *J. Chem. Phys.*, vol. 135, no. 14, 2011.

[59] T. M. Grehk, “Absorption of Li on the Si(100)2X 1 surface studied with high-resolution core-level spectroscopy,” vol. 52, no. 23, 1995.

[60] C. W. Ong, H. Huang, B. Zheng, R. W. M. Kwok, Y. Y. Hui, and W. M. Lau, “X-ray photoemission spectroscopy of nonmetallic materials: Electronic structures of boron and B x O y,” *J. Appl. Phys.*, vol. 95, no. 7, pp. 3527–3534, 2004.

[61] C. Song *et al.*, “High-conductive nanocrystalline silicon with phosphorous and boron doping,” *Appl. Surf. Sci.*, vol. 257, no. 4, pp. 1337–1341, 2010.

[62] C. D. Stinespring and J. C. Wormhoudt, “Surface studies relevant to silicon carbide chemical vapor deposition,” *J. Appl. Phys.*, vol. 65, no. 4, pp. 1733–1742, 1989.

[63] Y.Inoue, “Raman spectra of a-SiC,” vol. 48, no. 12, pp. 1071–1075, 1983.

[64] M. Boccard and Z. C. Holman, “Amorphous silicon carbide passivating layers for crystalline-silicon-based heterojunction solar cells,” *J. Appl. Phys.*, vol. 118, no. 6, 2015.

APPENDICES

A. XPS Results

Table 0.1. *Chemical bonding of B1s in literature*

Chemical bonding (B 1s)	*Binding Energy (eV)*	*FWHM*	*Structure*
β_r-B[60]	187.9		
β_r-B[60]	187.3		
B-B/B-Si [61]	186.0		B doped a-Si PECVD

Table 0.2. *Chemical bonding of Si2p in literature*

Chemical bonding (Si 2p)	*Binding Energy (eV)*	*FWHM*	*Structure*
Si-C bond in tetrahedral SiC[27]	100.5	1.5	
Si bond to sp2 C-C/C-H[27]	101	1.8	
Si-C bond in tetrahedral SiC[27]	100.4	1.3	
Si-Si/Si-H[27]	99.7		
Si-Si[53]	99.2	2.13	HWCVD aSiC:H
Si-C[53]	100.5	1.38	HWCVD aSiC:H
o-Si-C[53]	101.8		HWCVD aSiC:H
SiO_x[53]	103.2		HWCVD aSiC:H

Table 0.3. *Chemical bonding of C 1s in literature*

Chemical bonding (C 1s)	*Binding Energy (eV)*	*FWHM*	*Structure*
C-Si bond in tetrahedral SiC[27]	283.4	1.3	
Sp2 C-C/C-H bonds to Si[27]	284.6	1.5	
C-O-Si/C-Si-O bonds in oxycarbide [27]	285.6	1.2	
C-Si bond[28]	283.4		
C-Si bond[42]	283.5		RF Plasma Sputtered 400W,5Pa
C-Si bond[42]	280.75		RF Plasma Sputtered 200W,5Pa
C-Si [53]	283.2		HWCVD aSiC:H at C_2H_2 6 sccm
C-C[53]	284.6	2.1	HWCVD aSiC:H at C_2H_2 6 sccm
C-O-H[53]	286.4		HWCVD aSiC:H at C_2H_2 6 sccm
C=O[53]	288.4		HWCVD aSiC:H at C_2H_2 6 sccm
C-Si[19]	283.2		aSiC:H
C-C/C-H[19]	284.6		aSiC:H
C-O-H[19]	286.4		aSiC:H
C=O[19]	288.4		aSiC:H
C2H2/Si[62]	282.7		

e